The Cryosphere, 20, 4767–4786, 2026
https://doi.org/10.5194/tc-20-4767-2026

The Cryosphere Open Access EGU

Impact of meteorological and oceanographic conditions on the state of sea ice in Hornsund, Svalbard over 23 years

Vincent Papin[1], **Zuzanna M. Swirad**[2], **A. Malin Johansson**[3], **and Eirik Malnes**[4]

[1]Faculty of Sciences and Technologies, University of Toulon, Toulon, France
[2]Institute of Geophysics, Polish Academy of Sciences, Warsaw, Poland
[3]Department of Physics and Technology, UiT The Arctic University of Norway, Tromsø, Norway
[4]NORCE Research AS, Oslo, Norway

Correspondence: Zuzanna M. Swirad (zswirad@igf.edu.pl) and A. Malin Johansson (malin.johansson@uit.no)

Received: 24 March 2026 – Discussion started: 31 March 2026
Revised: 16 July 2026 – Accepted: 20 August 2026 – Published: 28 August 2026

Abstract. Sea ice in fjords affects local hydrography, ecosystems, glacier stability and coastal erosion. The full archive of historical SAR imagery at ∼ 50 m resolution (Envisat ASAR, RADARSAT-2 and Sentinel-1) capturing the Hornsund fjord, Svalbard was used to create an unprecedented set of near-daily binary ice/open water maps over the fjord area for 23 seasons (2002–2025). We observe a general trend with the sea ice season shortening by 2.3 d yr^{-1}, and a gradual decrease in average ice coverage, particularly in the main basin of Hornsund (−1.6 % yr^{-1}). The interannual ice condition variability was strongly related to the autumn (October–December) and/or winter (January–March) air temperatures. The length of the sea ice season was shortened by 19.5 d for every 1 °C increase in mean autumn air temperature ($R^2 = 0.61$, $p < 0.05$). After freeze-up, landfast ice in fjords predominantly forms level ice and was here found to be preconditioned by air temperature remaining under the freezing point for over 90 d and drift ice presence in the fjord with an average coverage exceeding 20 % 40 d before the landfast ice onset and 26 % 1 d before the onset. The landfast ice season break-up period was characterised by a lack of drift ice, and positive air temperatures for over a month. The day of landfast ice freeze-up and break-up overlapped with an average sea ice thickness of 0.33 and 0.57 m as derived from thermodynamic terms, respectively, suggesting the importance of other processes.

1 Introduction

Awareness of climate change has developed gradually over the decades, as scientific advances have enabled a better understanding of the impact of human activities on the climate. IPCC (2023) showed that the global surface temperature was 1.09 °C warmer during the period 2011–2020 compared to 1850–1900, primarily due to the greenhouse gases, dominated by carbon dioxide and methane, partially offset by the cooling effect of aerosols. The Arctic is one of the most affected regions, with a surface temperature increase of more than twice that of the global average, and with some regions experiencing even higher increases (Jansen et al., 2020). Since the beginning of satellite observations in 1978, sea ice coverage in the Arctic has significantly declined, reaching exceptionally low levels in September 2012 (https://nsidc.org/sea-ice-today/sea-ice-tools/charctic-interactive-sea-ice-graph; last access: 16 March 2026). Svalbard is one of the fastest warming regions in the world, with warming in both summer and winter being significant (van den Broek et al., 2025), which further warrants investigations of the state of the sea ice along the coast and within the fjords, and of the connections to changing meteorological and oceanographic conditions. Enclosed basins and fjords provide environments of level landfast ice formation (Galley et al., 2012), and the formation of the landfast ice as well as drift ice presence are essential for local breading and survival rates of seals and bird species (Smith and Lydersen, 1991; Sauser et al., 2023). Sea ice presence has been found to be one of the most important parameters for Svalbard seasonal glacier front behaviour (Li et al., 2025), with high correlations in southern Spitsbergen.

The reduction in sea ice cover contributes to the strengthening of surface winds, particularly in autumn and winter, most likely due to the lower surface roughness of open water compared to sea ice (Mioduszewski et al., 2018). This intensification of winds leads to increasing potential fetch and wave height in the region (Casas-Prat and Wang, 2020). These changes result in increased coastal exposure to wave-induced erosion (Zagórski et al., 2015; Herman et al., 2025). For Isfjorden, western Svalbard, the wind direction was found to affect the circulation pattern and hence the ocean surface water temperature (Fraser et al., 2018).

In addition to its environmental impact, sea ice plays a crucial role in Arctic navigation. The extent and thickness of sea ice directly affect the accessibility and safety of maritime routes in the polar region. Stocker et al. (2020) investigated the connection between maritime operations and the sea ice variability around Svalbard in 2012–2019, and found a clear correlation between the lack of sea ice and increased maritime operations. Though the behaviour differed between the fishing vessels and the cruise ships in change of location, where cruise ships sought to circumnavigate Spitsbergen and fishing vessels moved northwards.

In coastal Arctic environments, sea ice conditions often differ from those observed in the open ocean due to strong local controls. In sheltered bays landfast ice forms, but the factors influencing the formation and spatial extent of the landfast ice differ regionally and are not fully understood (Itkin et al., 2015). The steep surrounding topography, typical of Arctic fjords, can produce strong local contrasts in wind and near-surface air temperatures, leading to distinct microclimates that influence ice formation processes (Frank et al., 2023). Fjord hydrography is also complex, as oceanic inflows interact with freshwater input from glacier melt and river outflow, leading to stratification and circulation patterns that influence ice growth and break-up (Svendsen et al., 2002; Cottier et al., 2010). Beyond their environmental importance, coastal sea ice plays a crucial role for local transportation such as seasonal ice roads for community access, resource exploration and supply delivery (Dong et al., 2025). It also provides temporary protection against wave-driven coastal erosion (Swirad et al., 2026a). At the fjord scale, landfast ice is therefore not only a local expression of Arctic sea-ice change, but also a control on seasonal light availability, air-sea exchange, habitat conditions, glacier-front and mélange dynamics, and the degree of coastal exposure to waves.

This study focuses on the analysis of fjord ice conditions in Hornsund, Svalbard. The main objectives are threefold: (1) to produce binary ice/open water maps for Hornsund from the early 2000s up to the present day, thereby establishing a consistent long-term record of sea ice conditions; (2) to characterize sea ice and landfast ice seasons in terms of timing, duration and ice coverage; and (3) to identify the atmospheric and oceanic conditions that govern landfast ice freeze-up and break-up in the fjord. Through this approach, the study aims to improve our understanding of local-scale sea ice processes in Hornsund and contribute to a broader comprehension of how Arctic coastal systems respond to ongoing climatic changes.

2 Study area

Hornsund is one of the smallest fjords of Spitsbergen, the largest island of the Svalbard archipelago, located in its south-western part. It opens to the Greenland Sea in the west. The total area of Hornsund is about 320 km^2 with a width of 12 km and a length of 34 km. Its average depth is approximately 100 m, although the maximum depth can reach between 200–250 m in the main basin (Promińska et al., 2018).

The fjord consists of a main basin and several secondary bays, characterized by marine-terminating glaciers (Fig. 1). These bays are Burgerbukta (Vestre and Austre) in the north, Brepollen in the east and Samarinvågen in the south. Brepollen is about 12 km long, connected to the outer fjord by a 2 km wide entrance. Samarinvågen is 7 km long with an entrance 2 km wide, while Burgerbukta is 8 km long and has an entrance of 4 km. A sill at 40–50 m divides Brepollen and Samarinvågen from the main basin, significantly limiting water exchange between the two basins. Similarly there are sills at 25 and 30 m at the entrance to Austre and Vestre Burgerbukta, respectively (Jakacki et al., 2017).

There are 16 tidewater glaciers in Hornsund (Błaszczyk et al., 2023; Fig. 1). Between 2001 and 2010, the glaciers retreated at a rate of 70 $m\,yr^{-1}$ which is significantly higher than the 45 $m\,yr^{-1}$ average for Svalbard (Błaszczyk et al., 2013). This glacier retreat has led to an increase in the fjord's surface area, from 188 km^2 in 1936 to 303 km^2 in 2010, as well as in its length, from 24 km in 1936 to 34 km in 2010 (Błaszczyk et al., 2013). Swirad et al. (2026b) calculated a total Hornsund area gain of 30 km^2 between 2011 and 2023 resulting from glacier retreat.

Along the west coast of Spitsbergen, outside the fjords, the hydrological conditions and climate are mainly influenced by the West Spitsbergen Current (WSC) carrying warm (3.5–6.0 °C) saline ($>$ 35) Atlantic Water (AW) and the Sørkapp Current (SC) carrying cold (-1.5 to 1.5 °C) and fresher (34.3–34.8) Arctic Water (ArW) (Swerpel, 1985; Jakacki et al., 2017; Fig. 1b). The SC carries drift ice from the eastern part of the Svalbard Archipelago (Storfjorden) and the Barents Sea (Jakacki et al., 2017; Korhonen et al., 2024). In Hornsund, the presence of AW is relatively limited, however, Strzelewicz et al. (2021) reported an average annual increase of 8 % in the volume fraction of AW on the shelf between 1999 and 2020 with this trend becoming especially pronounced during the last decade, a process referred to as Atlantification.

In Hornsund, the water circulation is cyclonic (anticlockwise) with inflow from the southwest and outflow to the

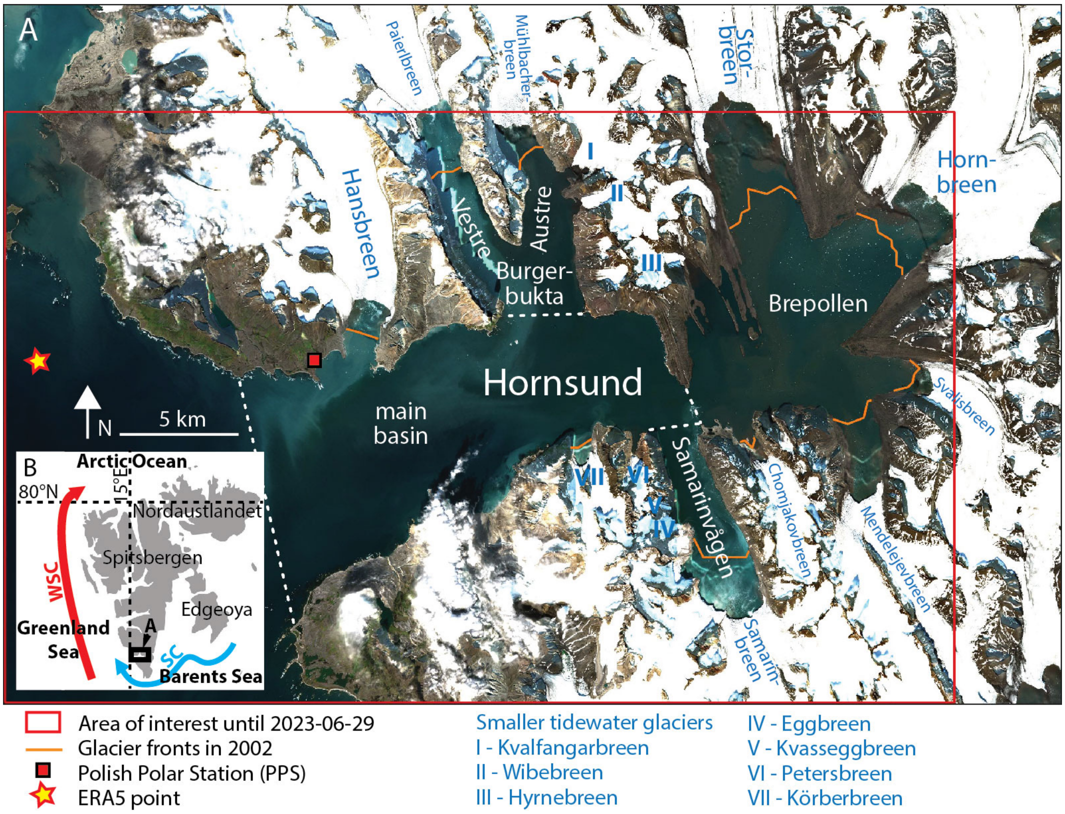

Figure 1. The study area: **(a)** Hornsund; **(b)** Svalbard. WSC: West Spitsbergen Current, SC: Sørkapp Current. Background image: Sentinel-2 T33XWF_20250828T120701_TCI_10m scene.

northwest. This circulation is mainly governed by tides and shelf currents (Jakacki et al., 2017). The tides are semidiurnal with an amplitude ranging between 0.8 and 1.8 m (Kowalik et al., 2015; Promińska et al., 2018). A statistically significant increase in storm frequency and the number of stormy days per year was observed at the decadal scale outside the fjord (Wojtysiak et al., 2018). The complex configuration of the Hornsund coastline and bathymetry causes strong wave modification through refraction and attenuation (Herman et al., 2019). The significant wave height, H_s, varies by location – it reaches 1.2–1.3 m at the fjord's entrance, decreases to 0.5–0.9 m in the central part, and falls below 0.4 m in the inner areas (Swirad et al., 2023b). Since 2006, the seasonal reduction in sea ice cover outside Hornsund has allowed more energetic waves to propagate into the fjord, increasing their impact on coastal zones (Herman et al., 2025).

Herman et al. (2025) suggested that the decline in sea ice cover at the fjord entrance led to changes in the spatial and seasonal distribution of wave energy. Zagórski et al. (2015) demonstrated shoreline retreat of 0.26 m yr^{-1} in Isbjørnhamna, where the Polish Polar Station (PPS) is located (Fig. 1b), between 1960 and 2011. This area shifted from a coastline formerly influenced by the nearby tidewater Hansbreen and the protection by persistent sea ice and glacier ice to one increasingly exposed to storms and that is undergoing rapid transformation (Zagórski et al., 2015). Additionally, the progressive degradation of permafrost and ground ice due to rising air temperatures reduces the mechanical strength of coastal sediments, making them more vulnerable to erosion (Dobiński and Kasprzak, 2022). Swirad et al. (2026a) observed near-zero net volume beach change in Isbjørnhamna between 2018 and 2025, but they observed existence of an erosional hotspot at the vicinity of the PPS infrastructure, and a net accumulation at the eastern part of the bay.

Between 1979 and 2018, the mean annual air temperature at the PPS meteorological station was −3.7 °C, with March being the coldest (−10.2 °C) and July – the warmest (4.6 °C). Monthly mean temperatures in summer months were relatively stable, typically around 5 °C, whereas winter months showed much greater fluctuations with means dropping below −10 °C (Wawrzyniak and Osuch, 2020). This strong seasonal variability in winter is attributed to alternating cold, stable anticyclonic subsidence and warmer, cyclonic disturbances (Rinke et al., 2017). The trend in mean annual air temperature over the study period was +1.14 °C per decade, which is more than five times higher than the global average warming rate of +0.17 °C per decade (NOAA, 2025; Wawrzyniak and Osuch, 2020). Dahlke et al. (2020) investigated the air temperature change from 1980–2016 for the whole of Svalbard, finding a significant warming over Hornsund for 2010–2016 in January–March compared to the climatological records, with a 1 °C per decade annual warming and a December–February warming of 2.8 °C per decade. Moreover, they found a statistically significant sea ice coverage reduction for the months of February–May for 1998–2016, a statistically significant reduction in May for 1980–1998, though no statistically significant change for 1980–2016. They also observed a reduced impact of wind and ice drift on the total sea ice extent around Svalbard, and that the surface air temperature has a larger impact on the extent.

3 Methods

3.1 Ice mapping

The entire archive of Envisat ASAR, RADARSAT-2 and Sentinel-1 synthetic aperture radar (SAR) imagery that fully covered Hornsund between 30 October 2002 and 31 August 2025 was used in this study (Table 1). The scenes were geocoded with a pixel size of 50×50 m and an WGS84, UTM33N extent of X: 499–544 km (901 pixels) and Y: 8531–8559 km (561 pixels) until the end of June 2023 and X: 498.9–549.1 km (1004 pixels), Y: 8530.9–8564.1 km (664 pixels) starting from July 2023, a change caused by glacier retreat north- and eastwards beyond the original area of interest (see Fig. 1). The Envisat ASAR was made up of a single channel (HH or VV) radar backscatter sigma nought and the incidence angle GeoTIFF rasters created using GASR software (Larsen et al., 2006). For RADARSAT-2 and Sentinel-1, both HH- and HV-channels radar backscatter sigma nought raster, as well as the incidence angle information were used.

A land mask was created using the Norwegian Polar Institute's land shapefile (NPI, 2014). The land mask was updated for each year on July 1st to account for tidewater glacier retreat and, hence, fjord area increase. Finally, a 100 m buffer was applied to exclude the tidal zone from the analysis (Swirad et al., 2024a).

To create binary maps of ice and open water, a segmentation algorithm was used. The algorithm was originally developed by Cristea et al. (2020) for open ocean and adapted to the Svalbard fjord environments by Johansson et al. (2020), and to Hornsund by Swirad et al. (2024a). This algorithm is based on a statistical model that accounts for surface-specific intensity decay with increasing incidence angle, a physical property particularly relevant for flat surfaces such as open water and sea ice (Johansson et al., 2020).

As input, the algorithm requires the incidence angle and one intensity channel, although multiple SAR intensity channels can be used. The HV-channel has lower return power, though is less affected by the wind influence on the water surface which can improve open water vs. sea ice separation compared to the HH-channel (Park et al., 2020; Zakhvatkina et al., 2017). However, this channel is limited by a low signal-to-noise ratio (SNR) (Park et al., 2020), and may not always improve the segmentation (Johansson et al., 2020; Zakhvatkina et al., 2017).

The algorithm is initialized with a single segment, which is iteratively optimized using an Expectation-Maximisation algorithm and evaluated with a Pearson-style goodness-of-fit (GOF) test. If the GOF criterion is not met, the segment is split. In cases where multiple segments exist, the least well-fitting segment is selected for division. This process continues until the algorithm reaches an optimal number of segments, defined as the lowest number that provides a sufficiently good fit to the data. A final contextual smoothing step, based on a Markov Random Field (MRF), is applied to improve spatial coherence and ensure simpler visual interpretation.

During the segmentation process, the images were multi-looked 3×3 and log-transformed, and the relevant land mask was used (Johansson et al., 2020; Swirad et al., 2024a). The multi-looking reduced speckle noise and enhanced contrast, while the logarithmic transformation helped approximate a Gaussian distribution of the data (Johansson et al., 2020).

Typically five (range: 3–6) discontinuous segments were automatically mapped. The segments were then manually classified as either "ice" or "open water" based on user experience and assumptions of (i) a better separation between open water and ice in the HV channel and (ii) a higher backscatter value for ice than open water under calm wind conditions (Johansson et al., 2020; Swirad et al., 2024a). Figure 2 shows an example of an original SAR scene, segmentation and classification.

Sentinel-1A/B imagery until June 2023 was processed by Swirad et al. (2024a), RADARSAT-2 imagery was processed by Swirad et al. (2026b). The present study contributed by extending the dataset from 11.5 years to nearly 23 years by adding the entire Envisat ASAR archive (Papin et al., 2025a) and Sentinel-1A imagery starting from July 2023 (Papin et al., 2025b), as well as by fixing erroneously processed Sentinel-1 images on 18 January 2015, 25 December 2018 and 12 February 2019 (Swirad, 2025).

Binary maps were combined into a single time series with a total of 4123 images spanning from 30 October 2002 to 31 August 2025, with an average frequency of 2.02 d. Consistency in ice detection between different sensors was previously verified (Johansson et al., 2020; Swirad et al., 2026b). When two images occurred on the same day, RADARSAT-2 was prioritised over Envisat ASAR and Sentinel-1 because of its lower noise floor. Validations of the SAR derived maps were carried out by Johansson et al. (2020) through comparisons with GPS tracks of the landfast ice edge and with manually drawn maps from the Zeppelin observatory in Ny-Ålesund, and by Swirad et al. (2024a) thorough comparisons of the landfast ice edge with 20 temporally and spatially overlapping Sentinel-2 optical images.

Table 1. Overview of the SAR imagery used in the study.

Sensor	Start date	End date	Number of images	Number of used images	Image frequency (days)	Binary maps URL
Envisat ASAR	30 Oct 2002	7 Apr 2012	1826	1061	3.25	https://doi.org/10.1594/PANGAEA.986427 (Papin et al., 2025a)
RADARSAT-2	2 Jan 2012	1 Mar 2016	797	638	2.38	https://doi.pangaea.de/10.1594/PANGAEA.969031 (Swirad et al., 2024b)
Sentinel-1	14 Oct 2014	29 Jun 2023	2967	2031	1.57	https://doi.org/10.1594/PANGAEA.963167 (Swirad et al., 2023a) Correction (3 images): https://doi.org/10.5281/zenodo.17350297 (Swirad, 2025)
	1 Jul 2023	31 Aug 2025	562	443	1.79	https://doi.org/10.1594/PANGAEA.987853 (Papin et al., 2025b)

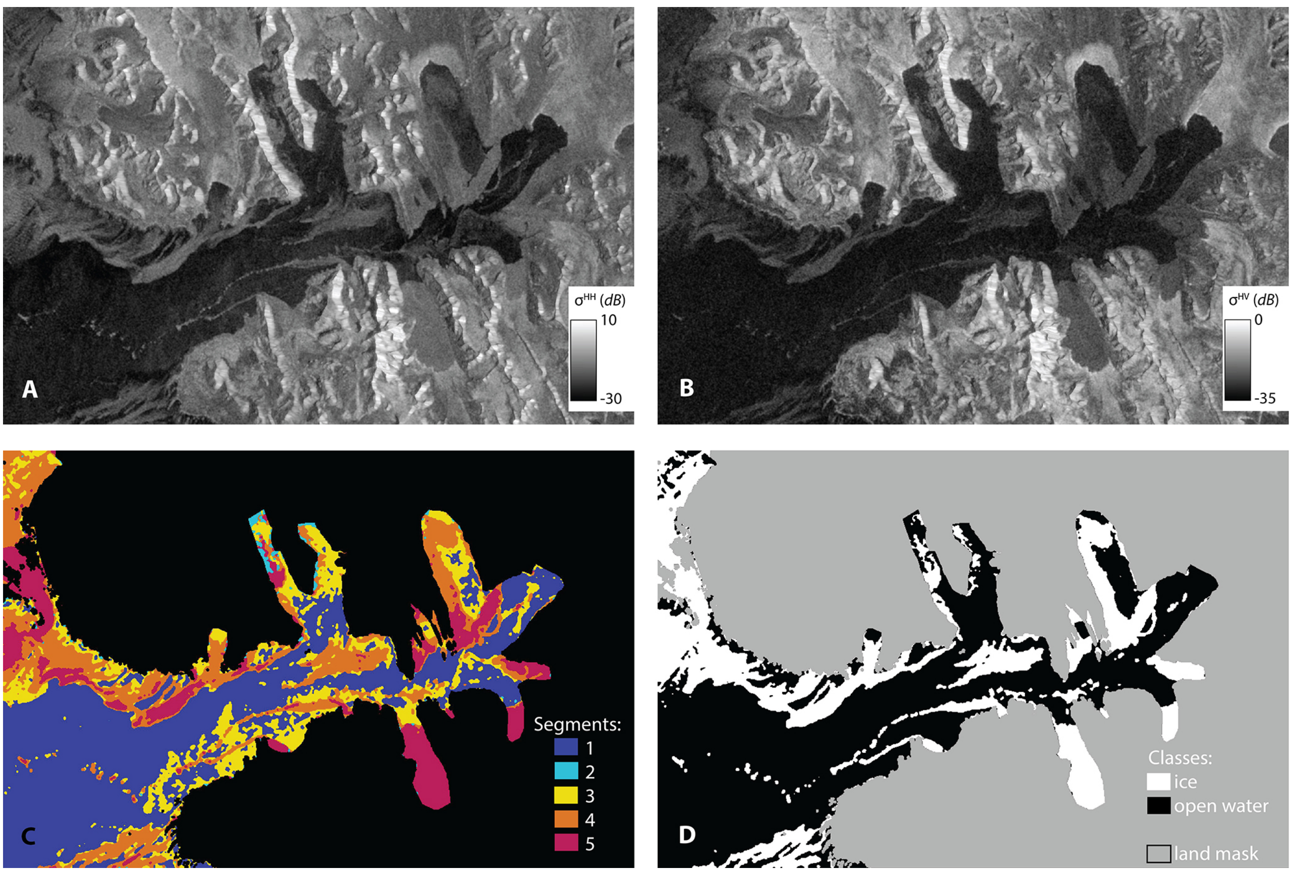

Figure 2. An example of the processing of the Sentinel-1 S1_EWM_20250119_054342_DES_037 scene: **(a)** HH backscatter intensity, **(b)** HV backscatter intensity, **(c)** segmented image, where 1 is the land mask and 2 to 6 are the discontinuous segments, **(d)** classified image.

3.2 Ice analysis

Binary ice/open water maps were used to characterise spatial and temporal ice conditions in Hornsund. Ice extent and coverage were calculated for the entire fjord as well as for the main basin and three main bays – Burgerbukta, Brepollen and Samarinvågen as delimited in Fig. 1. The coverage was calculated as the ice extent divided by the area of interest, which was updated annually on 1 July based on the landmask extent varied due to glacier front retreat.

The first and last day of the presence of drift and landfast ice inside the fjord were found visually in the SAR intensity images and the binary maps. The sea ice season was defined as the period between the first day of drift ice and landfast ice break-up, while the landfast ice season was delimited by the landfast ice freeze-up and break-up. The length of the sea ice and landfast ice seasons, and the average ice coverage during the sea ice and landfast ice seasons were calculated to identify interannual trends. The ice coverage was calculated for the entire fjord and for its parts – the main basin and the three main bays (Fig. 1) – to identify spatial trends. The seasonal analyses start on 1 September which is defined as the sea ice minimum date (Johansson et al., 2020).

3.3 Meteorological and oceanographic data

Air temperature data from 1 July 2002 to 31 August 2025 come from Vaisala HMP45D and HMP155 probes located 2 m above ground level (12 m a.s.l.), near the main buildings of the PPS, approximately 200 m from the shore. The mean hourly temperature was calculated by averaging hourly min and max values, as these two observations were the only ones available until 2008–2006. The mean daily air temperature (T) was calculated by averaging the mean hourly temperature. Mean daily wind speed (WS) was averaged from 1 min data with measurements performed with different instruments at a height of 10 m above the ground (around 20 m a.s.l.). For days with data gaps, the air temperature and wind speed was taken from the dataset provided by Wawrzyniak and Osuch (2020) for all dates before 1 January 2019, and thereafter linear interpolation of up to 7 d was applied.

Daily sea surface temperature (SST) and significant wave height (SWH) outside Hornsund were obtained from ERA5 reanalysis data (Hersbach et al., 2023) for the position 77° N, 15° E (see Fig. 1) at 12:00 UTC from 1 July 2002 to 31 August 2025. Data gaps, which generally overlap with sea ice concentration values over 30 %, were left blank.

T, WS, SST and SWH were subsequently averaged over three months to characterise summer (July–September), autumn (October–December), winter (January–March) and spring (April–June) for each year starting from summer 2002. The summer indicates the preceding summer.

T was also used to calculate the cumulative Freezing Degree Days (FDD) for the period leading to the landfast ice freeze-up and the cumulative Thawing Degree Days (TDD) for the period preceding the landfast ice break-up. FDD represents the sum of the negative temperature on days with degrees below the freezing point of seawater (−1.8 °C) starting from 1 September, and is defined by the formula given in Eq. (1):

$$\mathrm{FDD} = \int_0^t (T_\mathrm{f} - T(t))\mathrm{d}t \text{ for } T < T_\mathrm{f} \tag{1}$$

where t is time (days), $T_\mathrm{f} = -1.8\,°\mathrm{C}$ is the freezing temperature of seawater, and T is the mean daily air temperature (°C).

Similarly, TDD represents the cumulative sum of degree days with temperatures above 0 °C starting from the landfast ice freeze-up day, and is defined by Eq. (2):

$$\mathrm{TDD} = \int_0^t T(t)\mathrm{d}t \text{ for } T > T_0 \tag{2}$$

where T_0 is 0 °C, and T is the mean daily air temperature (°C).

FDD and TDD were also used to estimate the thermodynamically grown landfast ice thickness. To do so, we first calculated the combined effect of FDD and TDD after Su and Wang (2012) as:

$$\vartheta = \mathrm{FDD} - 3 \times \mathrm{TDD} \tag{3}$$

Although FDD and TDD are defined separately in Eqs. (1) and (2), both terms were calculated over the same seasonal period for the ice-thickness estimate so that intermittent freezing and thawing conditions were included through Eq. (3). Here, FDD and TDD were calculated for the same period, starting from the first day with $T < -1.8\,°\mathrm{C}$ and finishing on 31 August. Negative ϑ values were replaced by "0". We then calculated the ice thickness, SIT (m) using a formula by Lebedev (1938):

$$\mathrm{SIT} = 0.01333 \times \vartheta^{0.58} \tag{4}$$

The above-mentioned meteorological and oceanographic data were used to (1) characterize conditions during the 23 sea ice seasons and identify long-term trends, (2) find relationships (regression) between forcings and ice conditions (season length and ice coverage), and (3) describe environmental conditions leading to the landfast ice freeze-up and break-up.

4 Results

4.1 Ice conditions over the 23 seasons

The sea ice season began between October and March with the arrival of the drifting ice pack from the southwest, with a mean on 29 December. The landfast ice freeze-up occurred an average 28 d after the first drift ice, between December and March, with a mean on 26 January. The 2004/2005 and 2019/2020 seasons had the earliest and 2015/2016 had the latest drift ice arrival. The earliest landfast ice freeze-up occurred in the 2010/2011 and 2019/2020, and the latest in the 2015/2016. Drift ice was present in the fjord until April–July (average until 1 June), while the landfast ice broke up on average 23 d later, in May–July (mean on 24 June). The earliest end of both drift ice and landfast ice presence occurred in 2013/2014, and the latest in 2010/2011. The sea ice and landfast ice seasons lasted on average 178 and 150 d, respectively, being the shortest in 2015/2016 and the longest in 2004/2005 (sea ice season) or 2010/2011 (landfast ice season) (Table 2).

There was a gradual decrease in the length of the sea ice and landfast ice seasons of 2.34 and 0.66 d yr^{-1}, respectively, though the relationships are weak and statistically insignificant. The average ice coverage in Hornsund was 48 % during the entire sea ice season, but it was higher in the bays (66 %) and lower in the main basin (31 %). Earlier seasons (2002/2003 to 2010/2011) experienced higher ice coverage (≥ 53 %) with the exception of the 2005/2006 (31 %). From 2011/2012, the average ice coverage was more variable for from year to year, ranging from 12 % in 2013/2014 to 57 % in 2023/2024. Of the bays, Brepollen was characterized by the highest average ice coverage during the sea ice season (70 %), followed by Samarinvågen (69 %) and Burgerbukta (57 %). Similar trends characterised the landfast ice season. There was a statistically-significant negative trend in ice coverage in the main basin during the sea ice season (-1.63 % yr^{-1}, $R^2 = 0.32$, $p < 0.05$) and during the landfast ice season (-1.75 % yr^{-1}, $R^2 = 0.33$, $p < 0.05$) (Fig. 3).

On the day of the landfast ice freeze-up, the drift ice was typically present outside the fjord and in the main basin while landfast ice mostly started forming in Samarinvågen and southern Brepollen (Fig. 4a). During the landfast ice break-up the main basin was usually ice-free while the last landfast ice was present in Vestre Burgerbukta, northern Brepollen and depths of Samarinvågen (Fig. 4b).

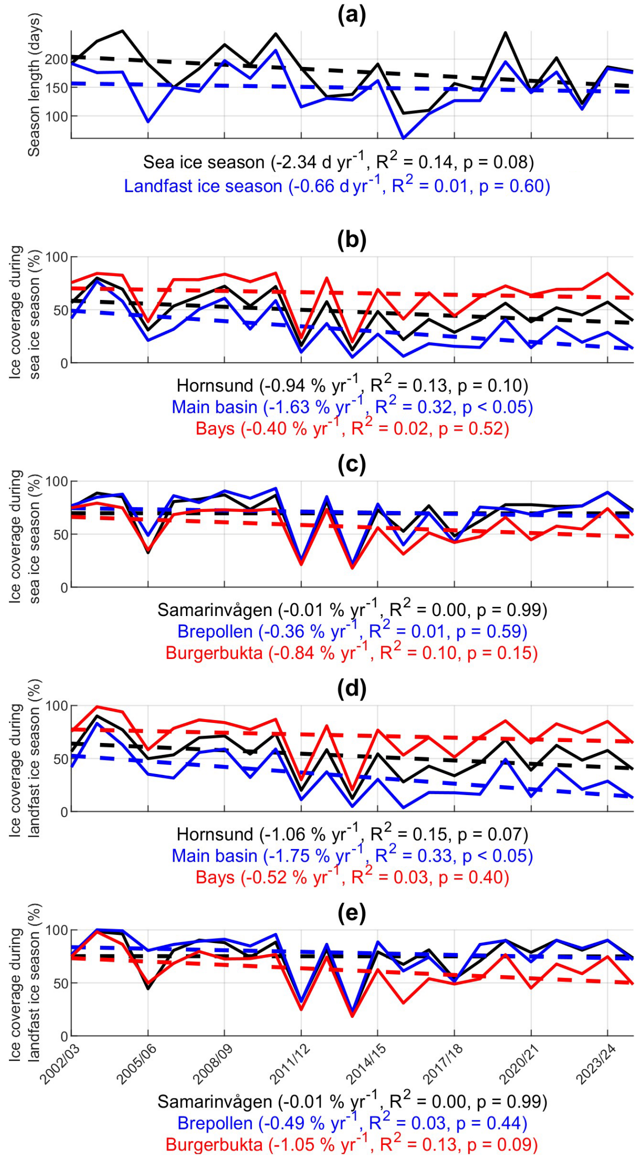

Figure 3. Time series of ice season parameters in Hornsund over the 23 seasons from 2002–2025: **(a)** the length of the sea ice season and the landfast ice season; average ice coverage during the sea ice season **(b)** for the parts of Hornsund, and **(c)** for individual bays; average ice coverage during the landfast ice season **(d)** for the parts of Hornsund, and **(e)** for individual bays.

4.2 Meteorological and oceanographic conditions

T averaged over the 23 seasons was 4.2 °C in summer, -3.6 °C in autumn, -8.0 °C in winter and -1.7 °C in spring. The first negative air temperatures in the fjord occurred between September and November, with the earliest recorded on 7 September 2002 and the latest on 1 November 2016. The last day of negative air temperature occurred between May and June, with the earliest on 20 May (2016 and 2022) and the latest on 12 June 2010.

WS was characterised by a high variability at a daily timescale. Seasonally, stronger winds were observed in winter (6.8 m s^{-1}) and autumn (6.2 m s^{-1}), compared to summer (4.6 m s^{-1}) and spring (5.4 m s^{-1}). SST was the lowest in winter (0.3 °C) and the highest in summer (4.2 °C). It averaged 1.2 °C in autumn and 0.9 °C in spring. The first negative SST values occurred between October and March, with the earliest recorded on 17 October 2005 and the latest on 28 March 2017. The last day with negative SST occurred between April and July, with the earliest on 1 April 2006 and the latest on 7 July 2004. SWH was the highest in winter (2.1 m), followed by autumn (1.8 m), spring (1.1 m), and summer (1.1 m).

There were four statistically-significant ($p < 0.05$) long-term seasonal trends in our dataset: increasing

Table 2. The timing and average ice coverage in Hornsund and its parts over the 23 sea ice seasons from 2002–2025.

Season	First day with drift ice	Landfast ice freeze-up	Last day with drift ice	Landfast ice break-up
2002/2003	2 Jan	2 Jan	9 May	12 Jul
2003/2004	13 Nov	7 Jan	30 Jun	30 Jun
2004/2005	27 Oct	7 Jan	18 Jun	2 Jul
2005/2006	3 Dec	14 Mar	10 May	11 Jun
2006/2007	31 Jan	31 Jan	26 Apr	29 Jun
2007/2008	8 Jan	17 Feb	3 Jul	8 Jul
2008/2009	23 Nov	20 Dec	30 May	5 Jul
2009/2010	26 Dec	19 Jan	3 Jul	3 Jul
2010/2011	19 Nov	18 Dec	20 Jul	20 Jul
2011/2012	11 Dec	17 Feb	6 Jun	11 Jun
2012/2013	8 Feb	11 Feb	4 Jun	21 Jun
2013/2014	2 Jan	12 Jan	9 Apr	19 May
2014/2015	29 Dec	27 Jan	13 Jun	7 Jul
2015/2016	15 Feb	30 Mar	26 May	29 May
2016/2017	1 Mar	7 Mar	18 May	18 Jun
2017/2018	30 Dec	29 Jan	23 May	4 Jun
2018/2019	25 Jan	12 Feb	3 Jun	18 Jun
2019/2020	28 Oct	18 Dec	26 May	29 Jun
2020/2021	2 Feb	4 Feb	8 Jun	24 Jun
2021/2022	3 Dec	28 Dec	23 May	22 Jun
2022/2023	11 Feb	21 Feb	24 May	12 Jun
2023/2024	1 Jan	4 Jan	29 Jun	4 Jul
2024/2025	10 Jan	12 Jan	30 Apr	6 Jul
Mean	29 Dec	26 Jan	1 Jun	24 Jun

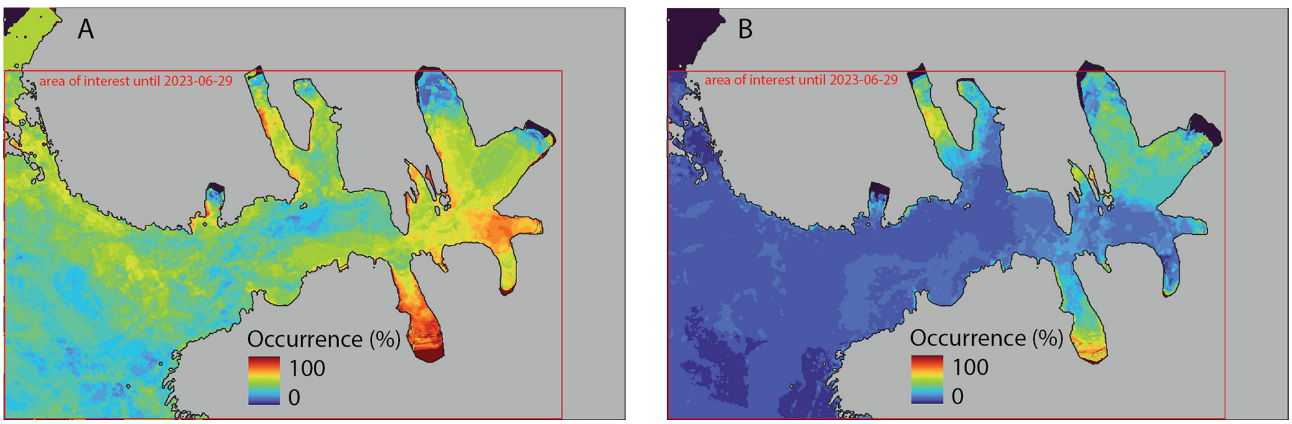

Figure 4. Mean distribution of ice on the **(a)** freeze-up and **(b)** break-up of the landfast ice in Hornsund over the 23 seasons from 2002–2025.

T_{summer} (+0.08 °C yr^{-1}, $R^2 = 0.59$), increasing WS_{summer} (+0.04 m s^{-1} yr^{-1}, $R^2 = 0.32$), decreasing WS_{winter} (−0.04 m s^{-1} yr^{-1}, $R^2 = 0.29$) and increasing SWH_{spring} (+0.01 m yr^{-1}, $R^2 = 0.21$) (Fig. 5).

4.3 Relationships between environmental conditions and the ice-season parameters

In general, longer and icier seasons were associated with colder autumns and winters. The 2003/2004 season had the highest ice coverage in Hornsund (80 % during the sea ice and 90 % during the landfast ice season), the lowest T_{autumn} (−7.6 °C), the third lowest T_{winter} (−11.0 °C), one of the highest WS_{winter} (7.4 m s^{-1}), the lowest SST_{spring} (−0.5 °C). The 2004/2005 season had the longest sea ice season (249 d), the second-highest ice coverage in the fjord during the landfast ice season (77 %), the earliest first drift ice (27 October), the lowest SST_{summer} (1.9 °C) and one of the highest WS_{winter} (7.4 m s^{-1}). The 2010/2011 season had the longest landfast ice season (215 d) related to the earliest landfast ice freeze-up (18 December) and the latest landfast ice break-up

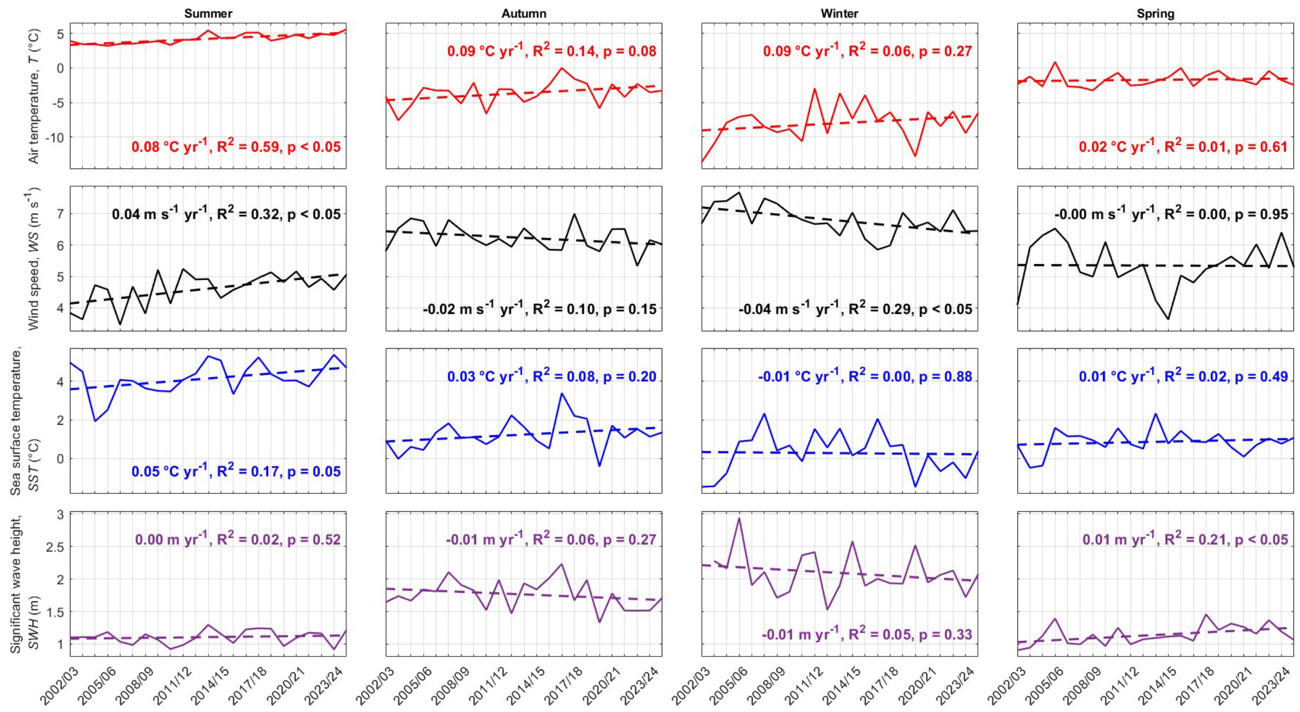

Figure 5. Seasonal averages of meteorological and oceanographic parameters in Hornsund for the 23 seasons from 2002–2025.

(20 July). T_{summer} was the second lowest (3.3 °C), and T_{winter} was one of the lowest (−10.6 °C). The 2019/2020 season also had the earliest landfast ice onset (18 December). Additionally, it had also one of the largest ice coverages, particularly in the bays (72 % during sea ice season and 85 % during landfast ice season). It was characterized by the lowest SST_{winter} (−1.5 °C), the lowest SST_{autumn} (−0.4 °C), and the lowest SWH_{autumn} (1.3 m).

The 2013/2014 season had the lowest ice coverage in Hornsund (12 % during both the sea ice and the landfast ice seasons) and its bays (20 % during the sea ice and 21 % during the landfast ice season), and the earliest end of the landfast ice season (19 May). This season had the highest SST_{spring} (2.3 °C), the highest SWH_{summer} (1.3 m) and the second highest T_{winter} (−3.7 °C). The 2015/2016 season had the shortest sea ice and landfast ice seasons (105 and 61 d, respectively), the latest landfast ice onset (30 March), and the lowest ice coverage in the main basin (3.6 %). This season was marked by the second highest T_{spring} (−3.2 °C). The 2016/2017 season had the latest occurrence of the first drift ice (1 March). It was also characterized by the highest T_{autumn} (−0.01 °C) and the lowest WS_{winter} (5.9 m s^{-1}) and it recorded the highest SST_{autumn} (3.4 °C), as well as the highest SWH_{autumn} (2.2 m).

Strong ($R^2 \geq 0.48$) statistically-significant ($p < 0.05$) negative relationships exist between T_{autumn} or T_{winter} and all considered characteristics of sea ice and landfast ice seasons (Fig. 6).

Stepwise linear regression relating environmental drivers to ice season parameters showed that using multiple predictors improved the fit (adjusted $R^2 \geq 0.73$, $p < 0.05$ for seven out of eight parameters) compared to a single predictor (Fig. 6 vs. Table 3). Predictors showing negative correlations with multiple ice season parameters are T_{winter}, T_{autumn}, T_{spring}, WS_{summer}, SST_{spring}, SST_{summer}, SWH_{summer}, SWH_{autumn} and SWH_{winter}. Conversely, a positive correlation links ice season parameters to WS_{winter}, WS_{autumn}, SST_{winter} and SST_{autumn} (Table 3).

4.4 Conditions leading to the landfast ice freeze-up and break-up

In the period leading to the onset of landfast ice, T gradually decreased (−0.1 °C d^{-1}, $R^2 = 0.81$, $p < 0.05$) with the average below the sea water freezing point for > 90 d (Fig. 7a). The 2009/2010 season had the highest mean T (−3.1 °C), while the 2003/2004 season had the lowest mean T during this 90 d period (−8.2 °C). The drift ice appeared on average 28 d earlier, ranging from 0 (2002/2003 and 2006/2007) and 101 d (2005/2006). Ice coverage during the period between first day with drift ice and the first day with landfast ice averaged 21 % with the minimum of 0 % in 2009/2010 (drift ice was present outside the fjord and no imagery was available between 26 December and 19 January for a better assessment) and the maximum of 85 % in 2008/2009 (Table 4). Ice coverage generally remained low during the early part, followed by an increase as the landfast ice freeze-up ap-

Table 3. Stepwise regression models of the ice-season parameters in Hornsund over the 23 seasons from 2002–2025.

Ice-season parameter	Best-fit model	Adjusted R^2	p value
Length of the sea ice season	$-135.76 - 5.09 \times T_{autumn} - 7.14 \times T_{winter} - 12.74 \times T_{spring} + 26.16 \times WS_{autumn} - 18.63 \times SST_{autumn} + 37.28 \times SWH_{winter}$	0.83	0.21
Average ice coverage in Hornsund during the sea ice season	$9.98 - 4.43 \times T_{winter} - 2.60 \times T_{spring} - 10.72 \times WS_{summer} + 10.45 \times WS_{winter} - 5.07 \times SST_{spring} - 8.51 \times SWH_{winter}$	0.89	7.04×10^{-6}
Average ice coverage in the main basin during the sea ice season	$23.63 - 6.31 \times T_{autumn} - 3.11 \times T_{winter} - 10.22 \times WS_{summer} + 5.82 \times WS_{winter} - 3.90 \times SST_{summer} + 7.23 \times SST_{autumn} + 3.30 \times SST_{winter} - 9.09 \times SST_{spring} - 16.42 \times SWH_{summer}$	0.91	4.80×10^{-4}
Average ice coverage in the bays during the sea ice season	$66.60 + 15.83 \times T_{summer} - 5.11 \times T_{winter} - 17.75 \times WS_{summer} - 5.56 \times WS_{autumn} + 17.79 \times WS_{winter} - 7.09 \times SST_{summer} + 8.37 \times SST_{autumn} - 7.12 \times SST_{spring} - 56.25 \times SWH_{summer} - 11.61 \times SWH_{winter}$	0.85	0.03
Length of the landfast ice season	$108.31 - 8.51 \times T_{autumn} - 5.97 \times T_{winter} - 14.18 \times T_{spring} - 34.71 \times SWH_{autumn}$	0.73	8.68×10^{-3}
Average ice coverage in Hornsund during the landfast ice season	$25.92 - 4.70 \times T_{winter} - 10.82 \times WS_{summer} + 8.32 \times WS_{winter} - 2.54 \times SST_{summer} - 6.84 \times SST_{spring}$	0.92	4.48×10^{-7}
Average ice coverage in the main basin during the landfast ice season	$-3.08 - 4.43 \times T_{autumn} - 4.13 \times T_{winter} - 10.75 \times WS_{summer} + 5.84 \times WS_{autumn} + 6.24 \times WS_{winter} - 3.23 \times SST_{summer} + 7.42 \times SST_{winter} - 10.11 \times SST_{spring} - 12.16 \times SWH_{autumn}$	0.92	3.66×10^{-3}
Average ice coverage in the bays during the landfast ice season	$84.21 - 5.16 \times T_{winter} - 9.58 \times WS_{summer} - 9.51 \times SST_{spring}$	0.79	3.00×10^{-5}

proached. The timing varied from year to year but 40 d before the freeze-up the average ice coverage exceeded 20 %. The average coverage of 26 % characterised the day before and 46 % the freeze-up day (Fig. 8). The period leading to the landfast ice freeze-up was also characterised by the gradual decrease of SST ($-0.02\,°\mathrm{C\,d^{-1}}$, $R^2 = 0.89$, $p < 0.05$) and an increase of WS ($+0.02\,\mathrm{m\,s^{-1}\,d^{-1}}$, $R^2 = 0.31$, $p < 0.05$) and SWH ($+0.004\,\mathrm{m\,d^{-1}}$, $R^2 = 0.21$, $p < 0.05$) (Fig. 7 c, e, g). Mean FDD on the freeze-up day was 501 °C days and mean ϑ was 403 °C days, the difference caused by T oscillation around the freezing and melting points at the beginning of the season (Table 4).

In the period leading to the landfast ice break-up T grew gradually ($+0.1\,°\mathrm{C\,d^{-1}}$, $R^2 = 0.97$, $p < 0.05$), exceeding 0 °C on average 38 d before the last day with landfast ice (Fig. 7b). Mean TDD on the break-up day was 89 °C days (Table 4). There was also a gradual decrease in WS ($-0.02\,\mathrm{m\,s^{-1}\,d^{-1}}$, $R^2 = 0.81$, $p < 0.05$) and SWH ($-0.01\,\mathrm{m\,d^{-1}}$, $R^2 = 0.63$, $p < 0.05$), and an increase in SST ($+0.03\,°\mathrm{C\,d^{-1}}$, $R^2 = 0.88$, $p < 0.05$) over 90 d leading to the landfast ice break-up (Fig. 7d, f, h).

4.5 Sea ice thickness

Calculation of sea ice thickness thermodynamic growth shows a large variability between the seasons (Fig. 9). In most seasons the ice formation started a few times with T oscillation around the freezing and melting points in autumn. In general, the earlier the start of ice growth the larger the maximal thickness and the longer the sea ice season. The largest thickness of 1.07 m was reached in the 2019/2020 season, followed by the 1.03 m in the first two seasons. The smallest thickness was observed in 2015/2016 (0.51 m) and 2011/2012 (0.60 m). For ten seasons the calculated thickness on 31 August was still positive despite the latest landfast ice break-up on 20 July (Fig. 9). The estimated ice thickness on the day when we visually established the landfast ice freeze-up in the SAR imagery and the binary maps averaged 0.43 m ranging from 0.31 to 0.60 m, and on the landfast ice break-up it was on average 0.71 m with the range of 0.46–0.97 m (Table 4).

Table 4. Conditions leading to the landfast ice freeze-up and break-up in Hornsund.

Season	Landfast ice freeze-up					Landfast ice break-up		
	Number of days with drift ice	Average ice coverage (%)	FDD (°C days)	ϑ (°C days)	Thermodynamic ice thickness (m)	TDD (°C days)	ϑ (°C days)	Thermodynamic ice thickness (m)
2002/2003	0	No Value	466	305	0.37	132	1407	0.89
2003/2004	55	57	766	706	0.60	60	1631	0.97
2004/2005	72	45	553	530	0.51	83	1236	0.83
2005/2006	101	7.6	717	576	0.53	80	597	0.54
2006/2007	0	No Value	546	450	0.46	89	894	0.69
2007/2008	40	16	553	493	0.49	107	1015	0.74
2008/2009	27	85	378	350	0.40	122	1291	0.85
2009/2010	24	0	326	229	0.31	76	887	0.68
2010/2011	29	48	503	502	0.49	196	1163	0.80
2011/2012	68	11	438	284	0.35	22	668	0.58
2012/2013	3	6.1	557	435	0.45	68	1163	0.80
2013/2014	10	9.9	527	503	0.49	22	987	0.73
2014/2015	29	13	527	372	0.41	132	728	0.61
2015/2016	44	14	634	395	0.43	32	447	0.46
2016/2017	6	16	618	412	0.44	58	825	0.66
2017/2018	30	8.2	309	260	0.34	52	804	0.65
2018/2019	18	3.8	561	381	0.42	77	816	0.65
2019/2020	51	10	430	412	0.44	118	1591	0.96
2020/2021	2	14	464	352	0.40	65	774	0.63
2021/2022	25	6.1	410	387	0.42	115	1184	0.81
2022/2023	10	6.8	452	333	0.39	50	730	0.61
2023/2024	3	23	371	325	0.38	132	997	0.73
2024/2025	2	39	415	273	0.35	150	652	0.57
Mean	28	21	501	403	0.43	89	978	0.71

5 Discussion

This study is the third of a series of articles that focus on sea ice conditions in the Hornsund fjord, Svalbard. The first publication (Swirad et al., 2024a) adapted a semi-automated method of Cristea et al. (2020) and Johansson et al. (2020) to create high-resolution (50 m) near-daily binary maps of ice and open water of Hornsund using the full Sentinel-1A/B archive available at the time. The main findings included (1) a large interannual variability in sea ice conditions without a clear trend over the nine analysed seasons, (2) differences in timing and extent of the ice cover in different parts of the fjord, notably the main basin and the inner bays, and (3) a presence of a secondary peak in ice coverage in the bays in autumn, that the authors attributed to the presence of glacier ice (Swirad et al., 2024a). The second study (Swirad et al., 2026b) expanded the dataset back in time to include the full RADARSAT-2 archive and developed a method to separate the ice into glacier ice, drift ice and landfast ice. The authors showed that the ice in Hornsund was 53 % drift, 35 % landfast, 8.5 % glacier ice, while the remaining 3.5 % was either unclassified or masked out. Statistically-significant negative correlations were found between winter (January-March) water temperature and the length of the sea ice and landfast ice seasons, and between winter air temperature and the mean coverage of sea ice (drift and landfast ice combined) and landfast ice. Glacier ice coverage was negatively correlated with summer air and autumn water temperatures. At the 12-season scale no long-term trends in ice conditions were detected (Swirad et al., 2026b). In this study we further extended the dataset in time – backward by using the full Envisat ASAR archive (Papin et al., 2025a) and forward by using subsequent Sentinel-1A imagery (Papin et al., 2025b). We supplemented the dataset with meteorological data from the PPS monitoring programme, and oceanographic data from ERA5 reanalysis for a location outside the fjord. Because of the strong ($R^2 = 0.95$–0.96) statistically-significant ($p < 0.05$) relationships between the extent of drift ice from Swirad et al. (2026b) and our ice extent in the main basin for both the sea ice and the landfast ice seasons, as well as between the landfast ice from Swirad et al. (2026b) and our ice extent in the bays (Fig. 10), we treat the differences between the main basin vs. the bays as a proxy for the differences between drift vs. landfast ice.

The extended daily, 50 m dataset adds a process-oriented perspective to these earlier studies by resolving not only long-term changes, but also the timing, spatial contrasts, and sequence of ice events within the fjord. In particular, it allows us to distinguish between drift-ice variability in the exposed main basin and landfast-ice formation and persistence in the sheltered bays, and to examine how drift ice, thermal forcing,

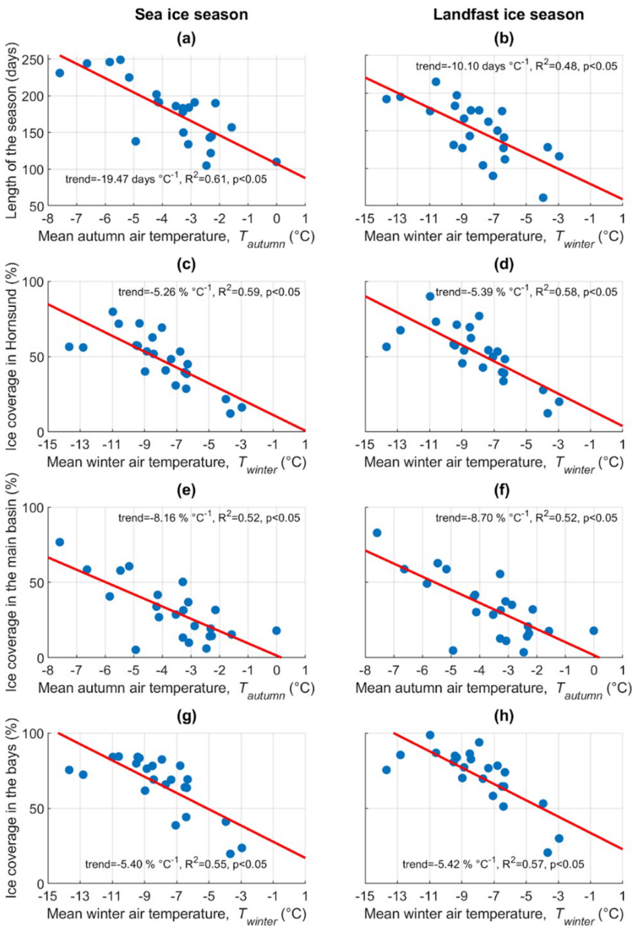

Figure 6. Linear correlations between the highest-correlation environmental driver (mean autumn or winter air temperature) and the ice-season parameters over the 23 seasons from 2002–2025: **(a–b)** length of the season; **(c–d)** average ice coverage in Hornsund; **(e–f)** average ice coverage in the main basin; **(g–h)** average ice coverage in the bays. The left panel represents the sea ice season and the right panel – the landfast ice season.

waves, and local fjord geometry interact during freeze-up and break-up.

Expanding the dataset to 23 seasons allowed us to observe the expected long-term decreasing trends in the length of ice season and in ice coverage, such as those observed in Svalbard by Onarheim et al. (2014), Dahlke et al. (2020) and Stocker et al. (2020), in Alaska by Mahoney and Einhorn (2026) and Jensen et al. (2020), and in the Canadian Archipelago by Gupta et al. (2022). The trends are stronger for the sea ice season compared to the landfast ice season, and for the main basin compared to the bays (Fig. 3). This suggests that mostly the pack ice is affected, as generally in the Arctic, while the state of the landfast ice may be more affected by local conditions, such as those of sheltered bays of eastern Hornsund. Notably, the variability of season length was more dependent on the start of the season (October–March) than on its end (May–July). The start of sea ice season is associated with the arrival of pack ice from the Barents Sea, while the end represents the disappearance of landfast ice. The unstable start vs. the stable end of the sea ice season further confirms that the drift ice is mostly affected. Araźny et al. (2018) observed a gradient in meteorological conditions (temperature and humidity) between the more maritime western and more continental eastern Hornsund. The Atlantification of Hornsund where the warmer and more saline AW becomes dominant over the cooler and fresher ArW (Strzelewicz et al., 2021) affects mostly the outer parts of Hornsund, while the inner bays remain highly affected by glacier outflow (Korhonen et al., 2024). Extended period between the first FDD and landfast ice formation was also found along the Alaskan coastline by Mahoney and Einhorn (2026), which they attribute to the warmer water temperatures in fall, equivalent to the Atlantification in Hornsund. Further indication on the positive effect of drift ice presence for landfast ice formation has also been observed in the Beaufort and Chukchi Seas (Mahoney et al, 2014). Glacier retreat, and the resulting bay deepening provides more and more sheltered conditions for the landfast ice to form and persist, with the katabatic winds, glacier ice floating in the bays and subsurface outflow further decreasing near surface water temperatures. As increased water depth is a limiting factor for landfast ice extent (Mahoney et al., 2014; Jensen et al., 2020), retreating glaciers can provide more stable and shallow water areas for ice formation. Combination of observed over the similar timescale as ours 8 % increase of AW volumetric fraction per year (Strzelewicz et al., 2021) and faster glacier retreat in Hornsund compared to other parts of Svalbard (Błaszczyk et al., 2013) further highlights the increasing local contrasts between the main basin and the bays, and between drift ice and landfast ice. This contrast between the main basin and the bays is one of the clearest process-related patterns revealed by the dataset. The main basin is more directly connected to incoming drift ice, shelf conditions, Atlantification and wave exposure, whereas the inner bays are partly decoupled from these external forcings and are more strongly influenced by local sheltering, glacier freshwater input, katabatic winds and bay geometry. The stronger decline in the main basin therefore indicates a response dominated by reduced drift-ice supply and increasing exposure to open-water conditions, while the weaker response in the bays reflects the persistence of locally controlled landfast-ice formation. Similarities between our observations with those in the Canadian Archipelago (Gupta et al, 2022) and along the Alaskan coastline (Mahoney et al., 2014; Jensen et al., 2020; Mahoney and Einhorn, 2026) puts this work into a larger Arctic Ocean context.

The decline of pack ice drifting to the entrance of Hornsund from the Barents Sea was also shown by Herman et al. (2025) for the 1979–2023 ERA5 reanalysis data, though the authors pointed to a "regime shift" after 2005 rather than a gradual change. A decline of the sea ice in Horn-

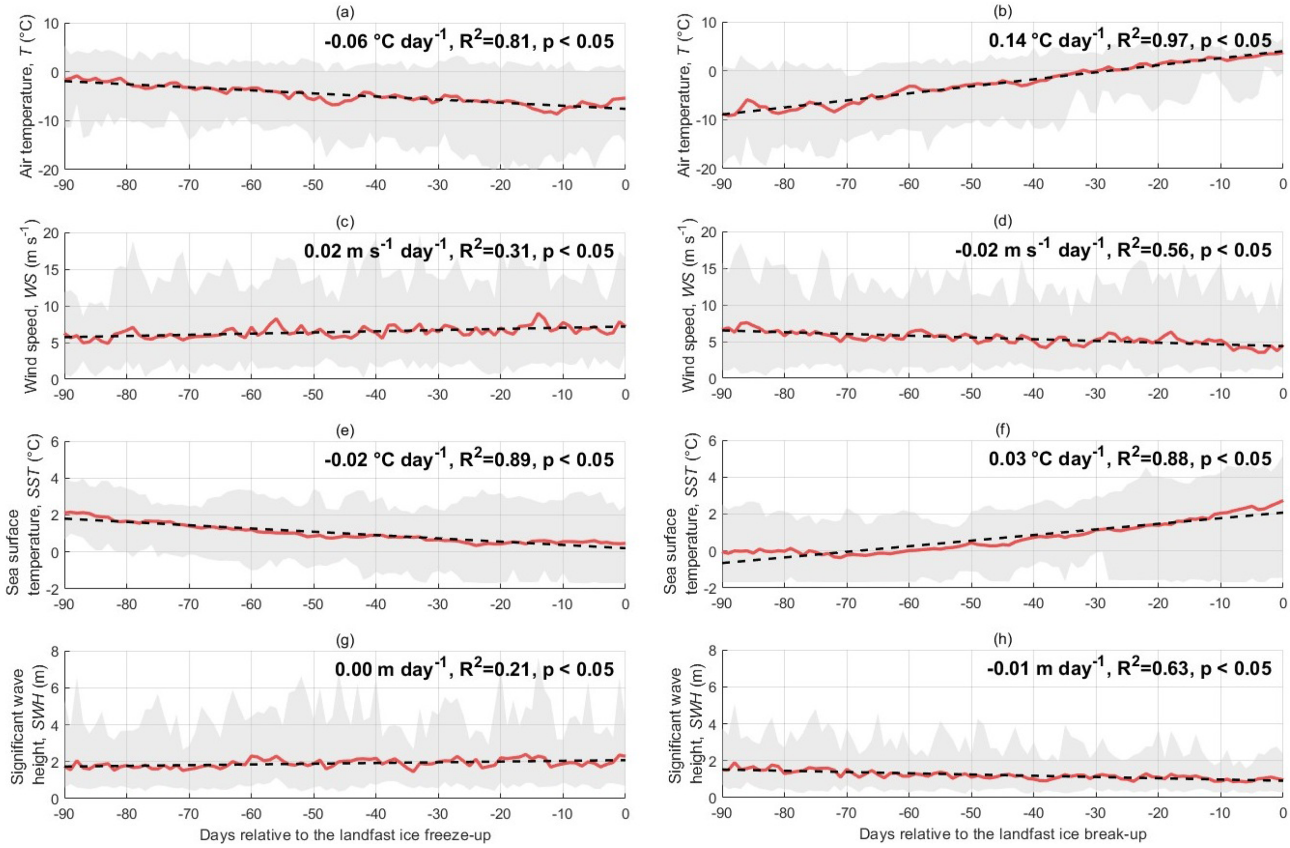

Figure 7. Evolution of **(a–b)** air temperature, T, **(c–d)** wind speed, WS, **(e–f)** sea surface temperature, SST, and **(g–h)** significant wave height, SWH, 90 d before the landfast ice freeze-up (left side) and break-up (right side) in Hornsund over the 23 seasons from 2002–2025.

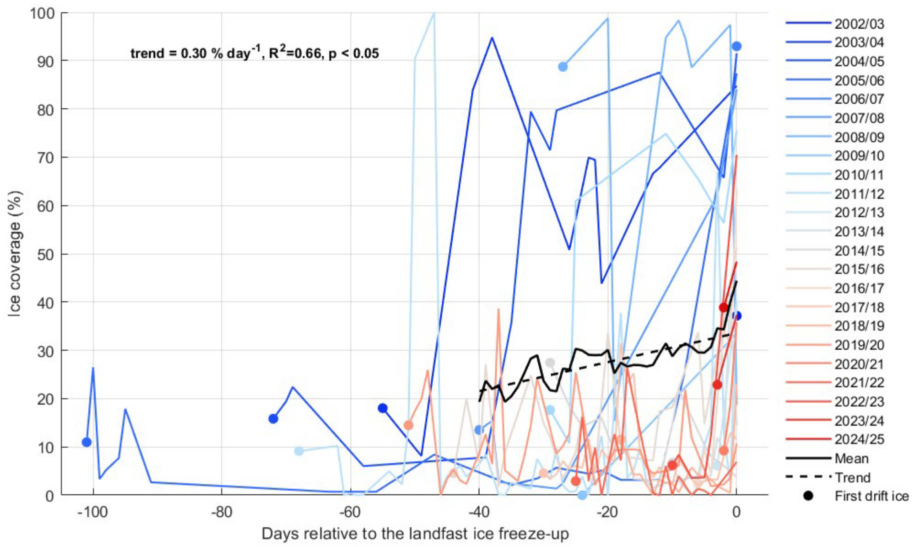

Figure 8. Ice coverage in Hornsund from the first drift ice to the landfast ice freeze-up over the 23 seasons from 2002–2025.

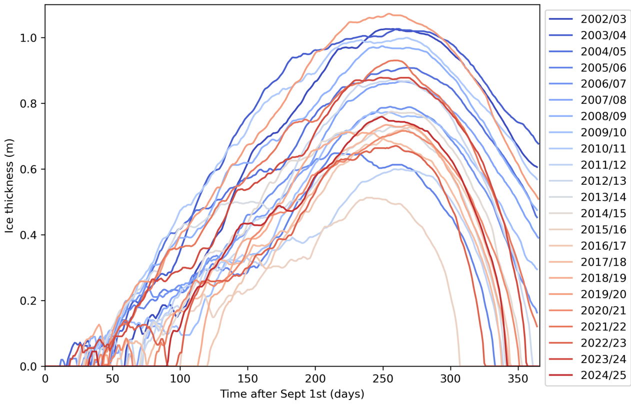

Figure 9. Time series of sea ice thickness in Hornsund calculated using the method of Su and Wang (2012) for the 23 seasons from 2002–2025.

sund was also shown by Muckenhuber et al. (2016) on the 2000–2014 optical and SAR imagery, though they identified icy periods of 2000–2005 and 2009–2011, and non-icy periods of 2006–2008 and 2012–2014, which could alternatively suggest warmer and colder periods of ∼ three years. Similar trends were observed in other fjords of Svalbard. For instance, Pavlova et al. (2019) documented an abrupt change in Kongsfjorden, where 2002/2003–2004/2005 were characterised with high sea ice coverage and the subsequent 2005/2006–2015/2016 had a reduced sea ice cover, with the minimum in 2011/2012. In Isfjorden, Muckenhuber et al. (2016) documented the abrupt change starting from the 2005/2006 season and the minimum sea ice coverage in 2011/2012 and 2013/2014. Finally, Johansson et al. (2020) observed a low sea ice coverage in Kongsfjorden in 2005/2006–2007/2008 and 2011/2012–2018/2019, and in Rijpfjorden in 2011/2012, 2015/2016 and 2017/2018.

Of the bays, Burgerbukta experienced the fastest decline of the ice coverage during the sea ice and landfast ice seasons, which is intuitive given its location in northern Hornsund, most exposed to the waves arriving from the south-west (Herman et al., 2019; Swirad et al., 2023b). We observed a gradual increase in air and water temperatures, particularly in autumn months (Fig. 5), which could decrease persistence (increase melting) of drift ice, as well as delay the in situ ice formation. Interestingly, there is a statistically-significant decline in winter wind speed. Wind has a complex effect on ice formation and persistence. Wind at the beginning of the sea ice season may accelerate ice production through accelerated ocean heat loss and ice deformation (Kwok, 2006). This phenomenon may become limited with decreasing wind speed, further contributing to slower in situ ice production. In the nearshore or fjord environment, cold katabatic winds from glaciers can decrease near surface water temperature in the bays enhancing the ice production. However, wind from the open sea will break up the forming landfast ice, particularly thin one at the beginning of the season.

On the top of the general trend of ice decline, there is a great variability in ice conditions from year to year that was already noticed in our previous studies (Swirad et al., 2024a, 2026b). The longest sea ice seasons and the largest ice coverage characterised the first three seasons (pre-regime shift) as well as two late seasons of 2019/2020 and 2021/2022. Conversely, the 2011/2012 and 2013/2014 remain the least icy seasons of the 21st century, while the 2015/2016 was the shortest (Table 2). These anomalous seasons can be interpreted as two types of outliers. The 2019/2020 and 2021/2022 seasons deviate from the long-term declining tendency by showing relatively extensive or persistent ice despite occurring late in the record. In contrast, seasons such as 2002/2003, 2011/2012, 2013/2014 and 2015/2016 deviate from the temperature-ice relationships shown in Fig. 6, indicating that air temperature alone does not explain the observed ice conditions. Such deviations likely reflect combinations of drift-ice supply, timing of cold periods, fjord-scale sheltering, wave exposure and spatial differences between the PPS meteorological station and ice-forming areas in the inner bays.

The seasonal ice parameters are strongly (R^2 of 0.48–0.61) correlated to T_{autumn} and T_{winter} (Fig. 6). T_{autumn} plays a major role for the length of the sea ice season and the ice coverage in the main basin during both the sea ice and landfast ice seasons, further pointing to the variability of drift ice conditions at the beginning of the season. Conversely, the length of the landfast ice season as well as the ice coverage in the bays respond mostly to T_{winter}, which is the period of landfast ice formation. Further corroborating the findings of Selyuzhenok et al. (2017) and Mahoney and Einhorn (2026) with the increase in time delay between the first FDD and landfast ice formation, T in the winter months through FDD widely controls ice thickness increase which then affects the time needed to melt/break-up the landfast ice at the end of the season. We found that all ice season parameters correlated better with T than water temperature, which matches the findings from Gupta et al. (2022) who found a clear correlation between T and the landfast ice formation. This result is different from that of our previous study (Swirad et al., 2026b), in which water temperature controlled the length of the season, and air temperature–ice coverage. We ascribe this difference to the duration of the study (23 vs. 12 seasons) as well as using SST of a point outside Hornsund (here) and seabed mooring data at 10–23 m depth (previous study). Deviation of points from the trendline in Fig. 6 suggests that T is not the only determinant of ice conditions. For instance, 2002/2003 had the lowest T_{winter}, but did not have the highest ice coverage. Similarly, 2011/2012, 2013/2014 and 2015/2016 all had the highest T_{winter}, but 2015/2016 had a considerably shorter landfast ice season (Fig. 6). Additionally, the meteorological station at PPS does not fully represent thermal conditions across the whole fjord (Araźny et al., 2018).

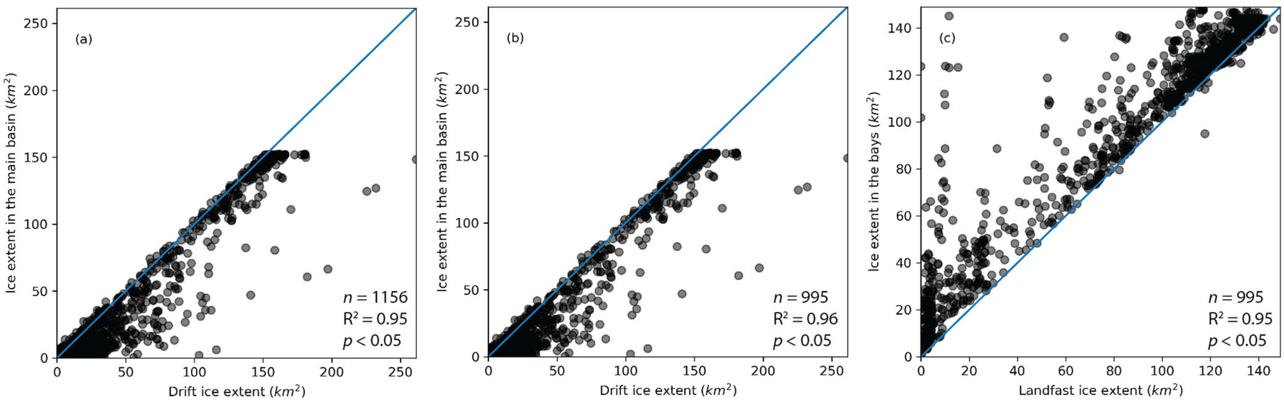

Figure 10. Spatial extent of the drift and landfast ice in Hornsund from Swirad et al. (2026b) and the ice extent in the main basin and the bays from our study on individual days between 2 January 2012 and 29 June 2023. Panel **(a)** represents the sea ice season and panels **(b)** and **(c)** the landfast ice season.

Multiple linear regression showed that combining multiple parameters allows a better fit (R^2 of 0.73–0.92) between the environmental and the eight ice season parameters than using a single variable (Table 3). T_{autumn} and T_{winter} were still the most important, but other parameters were also included (Table 3). The impact of SST was similar though weaker than T. For six ice parameters, $\text{WS}_{\text{summer}}$ was important, showing a negative correlation, though the physical meaning seems unclear. The positive relationship between $\text{WS}_{\text{autumn}}$ and the length of the sea ice season supports the acceleration of ice production through deformation (Kwok, 2006). We did not find any negative relationships between $\text{WS}_{\text{spring}}$ and/or $\text{SWH}_{\text{spring}}$ and ice season parameters to support the hypothesis of faster landfast ice break-up and melting by wind waves (Graham et al., 2019). SWH was generally the least important factor, which we justify by wave transformation at the entrance and inside the fjord which prevents direct comparison between the value from a single point outside the fjord and ice conditions in the fjord itself. However, when present, the relationship was negative which supports that waves break ice contributing to the shortening of the season and decrease of ice extent (Table 3). Long-term monitoring of water temperature and wave parameters could allow for more direct relationships to be identified. An alternative approach to describing environmental conditions, rather than using fixed 3-month seasonal averages, could be explored to improve model fit (Lei et al., 2012).

We also observed a temporal shift in ice phenomena over the years. The first seasons (pre-regime shift, i.e. until 2005) were characterised by a rapid increase in ice coverage between December and January, later it was from January to February, and in some years from February to March (Fig. S3 in the Supplement). This is similar to the observations by Mahoney and Einhorn (2026) for the Alaskan coastline. In consequence, Hornsund shores are more exposed to storm waves, and the hazard of coastal flooding and erosion is higher. Zagórski et al. (2015) pointed to autumn as a season of limited ice cover and large waves. However, our results suggest that December-February may be critical months, both because it is the season with the most intense storms (Swirad et al., 2023b) and because it experiences significant ice decline. Glacier calving and glacier ice accumulation in the bays, despite glacier retreat between June and October–December (Błaszczyk et al., 2023), may not level this shift. Glacier ice tends to be spread or grouped in belts, and it does not attenuate wave energy as efficiently as sea ice; it may also serve as abrasive tool, e.g. when moving up and down the shore with waves (Swirad et al., 2026a). Swirad et al. (2026b) observed a negative correlation between glacier ice coverage and both the glacier calving (approximated by the increase of annual land mask) and the summer air and autumn water temperatures, which suggests that although fewer growlers and bergy bits are expelled from glacier fronts during cold summers/autumns, they persist in the fjord for longer. Li et al. (2025) observed that for southern Svalbard the peak in air temperature occurred in late June, followed by a peak in water temperatures in August and a peak in glacier retreat in September, showing a clear trend between the water temperatures and the glacier retreats.

Suitable conditions for the landfast ice formation include the presence of drift ice (Figs. 4 and 8) that attenuates waves and lowers near-surface water temperature, and extended period of cold air temperatures. As temperatures may return to the melting point a few times before the landfast ice onset, ϑ, the cumulative effect of FDD and TDD starting from the first day below $-1.8\,°\text{C}$, seems to better reflect conditions necessary for water freezing than FDD alone. This is corroborated by finding along the Alaskan coastline by Mahoney and Einhorn (2026) that in their 27-year data record (1996–2023) found a delay in time between the first FDD and landfast ice formation. The minimal ϑ on the day of the landfast ice freeze-up was 229 °C days (Table 4). The ice thickness calculated in thermodynamic terms (Lebedev, 1938) for the landfast ice freeze-up day was on average 0.43 m, which may indicate a minimum thickness needed for ice detection using C-band SAR imagery. New SAR missions, the recently launched NISAR (NASA-ISRO) mission and upcoming ROSE-L (ESA), are carrying the L-band sensors with the free and open data policy, and in early March 2026 there were already approx. 180 NISAR images collected over Hornsund. Wakabayashi et al. (2004) showed a relationship between the L-band SAR backscatter values and sea ice thickness from approx. 5–10 cm thickness. For earlier years, it is possible that the landfast ice onset could be visible on SAR imagery earlier, but the lower temporal resolution of Envisat ASAR imagery resulted in a less accurate start date for the freeze-up. However, the seasons with the largest data gap before the landfast ice onset represented both thinner (2009/2010, 2002/2003) and thicker (2003/2004) than average ice (Table 5). The daily temporal resolution also clarifies the sequence of processes leading to freeze-up. Drift ice typically appears before landfast ice forms and may precondition freeze-up by reducing wave exposure and cooling near-surface waters. Stable landfast ice then initiates preferentially in sheltered bays, where local topography and reduced exposure favour persistence. The effect of local conditions on fast ice formation was also observed by Gupta et al. (2022) in the Canadian Archipelago. Conversely, break-up occurs after drift ice has disappeared from the fjord, leaving the remaining landfast ice increasingly exposed to positive air temperatures and suggesting that mechanical forcing from waves and locally generated wind seas may contribute to final break-up. Because landfast-ice freeze-up and break-up may respond to short-lived dynamic events, the 90 d tendencies in wind speed were interpreted together with absolute wind-speed conditions during the days immediately preceding each event. Mean and maximum wind speeds over short preceding windows provide a more direct indication of calm conditions during freeze-up and potential wind-driven mechanical forcing during break-up than wind-speed trends alone. Monitoring of wind speed strength and direction in individual bays could help find wind parameters preconditioning the landfast ice break-up.

Notably, calculating ice thickness using Eqs. (3) and (4) involves several assumptions and limitations which need to be taken into account when interpreting the results, as the estimates are limited to uninterrupted thermodynamic growth only. These equations do not explicitly include snow insulation or snow loading, oceanic heat-flux variability, basal melt, deformation, ridging or rafting, and they rely on air temperature measured at a single coastal station. These uncertainties are particularly relevant when comparing the estimated thickness with the observed timing of landfast ice freeze-up and break-up. The present calculations are, therefore, only an estimate intended to highlight the importance of other processes. The landfast ice break-up coincided with the time when pack ice was already absent (Fig. 8) and temperatures remained over the melting point for ca. 25 d. Interestingly both ϑ and thermodynamic ice thickness remained positive which may suggest that other processes play a key role in ice break-up. We suggest that these are waves, both swell/sea from the south-west and those locally generated by wind, that break the edges of the landfast ice and accelerate melting (Graham et al., 2019). The thermodynamic ice thickness at the time of the landfast ice break-up averaged 0.71 m. In situ ice thickness measurements, as well as local meteorological stations and moorings in the individual bays of Hornsund would help prove this hypothesis, enabling to account for local-scale differences in meteorological and oceanographic conditions, given the east-west gradient (Araźny et al., 2018) and topographic complexity.

Table 5. Dates and number of days with no data before/after the landfast ice freeze-up/break-up in Hornsund.

Season	Number of days with no data before landfast ice freeze-up	Number of days with no data after landfast ice break-up
2002/2003	36	0
2003/2004	11	39
2004/2005	1	7
2005/2006	7	8
2006/2007	8	3
2007/2008	2	1
2008/2009	0	0
2009/2010	23	2
2010/2011	1	1
2011/2012	0	0
2012/2013	2	2
2013/2014	0	0
2014/2015	1	2
2015/2016	4	3
2016/2017	0	1
2017/2018	0	0
2018/2019	0	0
2019/2020	0	0
2020/2021	0	0
2021/2022	3	5
2022/2023	3	1
2023/2024	2	0
2024/2025	1	0

6 Conclusions

The full archive of high-resolution SAR imagery (Envisat ASAR, RADARSAT-2 and Sentinel-1) fully covering Hornsund fjord between October 2002 and August 2025 was used to create an unprecedented set of near-daily binary ice/open water maps over the fjord area for 23 seasons. We observed a general trend of sea ice season shortening by 2.3 $d\,yr^{-1}$, and a gradual decrease in average ice coverage during the sea ice season, particularly in the main basin of Hornsund ($-1.6\,\%\,\mathrm{yr}^{-1}$), which we attributed to the general decrease in pack ice duration and extend in the Arctic. The changes are smaller down to negligible for the landfast ice season and the inner bays of the fjord, where landfast ice develops in situ. On the top of the longer-term trend, the results suggest a great interannual variability in ice conditions, which are strongly related to the autumn (October–December) and/or winter (January–March) air temperatures averaged from the observations at the Polish Polar Station. The length of the sea ice season is shortened by 19.5 d for every 1 °C increase in the mean autumn air temperature ($R^2 = 0.61$, $p < 0.05$). Step-wise multiple linear regression showed that predicting ice conditions can be improved by combining a range of meteorological and oceanographic parameters (air temperature, T, wind speed, WS, sea surface temperature, SST and significant wave height, SWH) with SST having a similar but more subtle effect than T, higher autumn WS characterising longer ice seasons and SWH showing weak but negative correlation with the ice conditions.

In the period leading to the landfast ice freeze-up, T typically remained under the freezing point (−1.8 °C) for over 90 d, decreasing gradually by $-0.1\,°\mathrm{C\,d}^{-1}$. At that time, the drift ice was present in the fjord, lowering the near surface water temperature and protecting fjord waters from the incoming wave energy. In average, for 40 d prior to the landfast ice formation the ice coverage exceeded 20 %, rising to 26 % on the day preceding the freeze-up. The landfast ice break-up was characterised by a lack of drift ice and positive T for an average of 38 d with a gradual increase of $0.1\,°\mathrm{C\,d}^{-1}$ over the 90 d period. Calculation of the sea ice thickness in thermodynamic terms showed that the landfast ice is detectable on C-band SAR imagery when it is thicker than 0.43 m (range: 0.31–0.60 m) while the landfast ice break-up is related to other processes than only melting (such as breaking by waves) since on the date identified as the landfast ice season end the thermodynamic thickness averaged 0.71 m.

This study provides open long-term (23 seasons) high spatial (50 m) and temporal (2 d) resolution dataset of ice maps for any analyses including fjord hydrography, glacier/ocean interaction and ecology. It can help assess wave impact on coastal change and safety for boat and snowmobile operations. Finally, because of its duration and detail, it provides information on the changing climate of the Arctic and the impact of weather and oceanic conditions on the state of ice.

Data availability. The binary ice/open water maps are available in the PANGAEA repository: those based on Envisat ASAR 2002–2012 are at https://doi.org/10.1594/PANGAEA.986427 (Papin et al., 2025a), those based on RADARSAT-2 2012–2016 are at https://doi.org/10.1594/PANGAEA.969031 (Swirad et al., 2024b), those based of Sentinel-1A/B 2014–2023 are at https://doi.org/10.1594/PANGAEA.963167 (Swirad et al., 2023a), and those based on Sentinel-1A 2023–2025 are at https://doi.org/10.1594/PANGAEA.987853 (Papin et al., 2025b). Additionally, three erroneously classified images from Swirad et al. (2023a) are available at https://doi.org/10.5281/zenodo.17350297 (Swirad, 2025).

Supplement. Table S1 in the Supplement is the time series of the extent and coverage of ice in Hornsund and its parts. Table S2 in the Supplement is a time series of meteorological and oceanographic conditions. Table S3 in the Supplement is a summary of ice and climate parameters for individual seasons. Document S4 contains supplementary figures. The supplement related to this article is available online at https://doi.org/10.5194/tc-20-4767-2026-supplement.

Author contributions. ZMS and AMJ conceptualised the study. EM pre-processed the SAR scenes. VP processed and analysed the data with the help from ZS. VP and ZS wrote the original manuscript. All authors edited the manuscript and agreed on its final version.

Competing interests. The contact author has declared that none of the authors has any competing interests.

Disclaimer. Publisher's note: Copernicus Publications remains neutral with regard to jurisdictional claims made in the text, published maps, institutional affiliations, or any other geographical representation in this paper. The authors bear the ultimate responsibility for providing appropriate place names. Views expressed in the text are those of the authors and do not necessarily reflect the views of the publisher.

Acknowledgements. We thank Meri Korhonen (IG PAS) for preparing meteorological data. Envisat ASAR and Sentinel-1 data are freely available through the European Union's Earth observation Copernicus programme (https://copernicus.eu, last access: 21 July 2025). RADARSAT-2 data was provided by NCS/KSAT under the Norwegian-Canadian RADARSAT-2 agreement 2011–16. ERA5 data are freely available at the Climate Data Store website (https://cds.climate.copernicus.eu/, last access: 17 November 2025).

Financial support. This study was funded by the European Space Agency (HIRLOMAP ESA Contract No. 4000146036/24/I-DT-bgh). Vincent Papin's stay at IG PAS was partly funded by the European Union's Erasmus programme. Eirik Malnes was partly funded by the European Space Agency (Svalbard Cryosphere Digital Twin – SvalbardDT, ESA Contract No. 4000146232/24/I-KE). The publication charges for this article have been funded by a grant from the publication fund of UiT The Arctic University of Norway.

Review statement. This paper was edited by Stephen Howell and reviewed by Ruibo Lei and one anonymous referee.

References

Araźny, A., Przybylak, R., Wyszyński, P., Wawrzyniak, T., Nawrot, A., and Budzik, T.: Spatial variations in air temperature and humidity over Hornsund fjord (Spitsbergen) from 1 July 2014 to 30 June 2015, Geografiska Annaler Series a Physical Geography, 100, 27–43, https://doi.org/10.1080/04353676.2017.1368832, 2018.

Błaszczyk, M., Jania, J. A., and Kolondra, L.: Fluctuations of tidewater glaciers in Hornsund fjord (southern Svalbard) since the beginning of the 20th century, Pol. Polar Res., 34, 327–352, 2013.

Błaszczyk, M., Moskalik, M., Grabiec, M., Jania, J., Walczowski, W., Wawrzyniak, T., Strzelewicz, A., Malnes, E., Lauknes, T. R., and Pfeffer, W. T.: The response of tidewater glacier Termini positions in Hornsund (Svalbard) to climate forcing, 1992–2020, J. Geophys. Res.-Earth Surf., 128, https://doi.org/10.1029/2022jf006911, 2023.

Casas-Prat, M. and Wang, X. L.: Projections of extreme ocean waves in the Arctic and potential implications for coastal inundation and erosion, J. Geophys. Res.-Oceans, 125, e2019JC015745, https://doi.org/10.1029/2019JC015745, 2020.

Cottier, F. R., Nilsen, F., Skogseth, R., Tverberg, V., Skarðhamar, J., and Svendsen, H.: Arctic fjords: a review of the oceanographic environment and dominant physical processes, Geological Society London Special Publications, 344, 35–50, https://doi.org/10.1144/sp344.4, 2010.

Cristea, A., Van Houtte, J., and Doulgeris, A. P.: Integrating incidence angle dependencies into the Clustering-Based Segmentation of SAR images, IEEE J. Sel. Top. Appl. Earth Obs., 13, 2925–2939, https://doi.org/10.1109/jstars.2020.2993067, 2020.

Dahlke, S., Hughes, N., Wagner, P, Gerland, S., Wawrzyniak, T., Ivanov, B., and Maturilli, M.: The observed recent surface air temperature development across Svalbard and concurring footprints in local sea ice cover, Int. J. Climatol., 40, 5246–5265, https://doi.org/10.1002/joc.6517, 2020.

Dobiński, W. and Kasprzak, M.: Permafrost base degradation: characteristics and unknown thread with specific example from Hornsund, Svalbard, Front. Earth Sci., 10, https://doi.org/10.3389/feart.2022.802157, 2022.

Dong, Y., Xiao, P., Zhang, X. Ge, D., Yu, J., Chen, Y., Wu, Q., Ma, Y., Liu, R., Luan, W., Liu, H., and Bai, J.: Increased vulnerability of Arctic potential ice roads under climate change, Commun. Earth Environ., 6, 37, https://doi.org/10.1038/s43247-025-02011-y, 2025.

Frank, L., Jonassen, M. O., Skogseth, R., and Vihma, T.: Atmospheric climatologies over Isfjorden, Svalbard, J. Geophys. Res.-Atmos., 128, https://doi.org/10.1029/2022jd038011, 2023.

Fraser, N. J., Skogseth, R., Nilsen, F., and Inall, M. E.: Circulation and exchange in a broad Arctic fjord using glider-based observations, Polar Res., 37, 1485417, https://doi.org/10.1080/17518369.2018.1485417, 2018.

Galley, R. J., Else, B. G. T., Howell, S. E. L., Lukovich, J. V., and Barber, D. G.: Landfast Sea Ice Conditions in the Canadian Arctic: 1983–2009, Arctic, 65, 133–144, https://doi.org/10.14430/arctic4195, 2012.

Graham, R. M., Itkin, P., Meyer, A., Sundfjord, A., Spreen, G., Smedsrud, L. H., Liston, G. E., Cheng, B., Cohen, L., Divine, D., Fer, I., Fransson, A., Gerland, S., Haapala, J., Hudson, S. R, Johansson, A. M., King, J., Merkouriadi, I., Peterson, A. K., Provost, C., Randelhoff, A., Rinke, A., Rösel, A., Sennéchael, N., Walden, V. P., Duarte, P., Assmy, P., Steen, H., and Granskog, M. A.: Winter storms accelerate the demise of sea ice in the Atlantic sector of the Arctic Ocean, Sci. Rep., 9, 9222, https://doi.org/10.1038/s41598-019-45574-5, 2019.

Gupta, K., Mukhopadhyay, A., Babb, D. G., Barber, D. G., and Ehn, J. K.: Landfast sea ice in Hudson Bay and James Bay: Annual cycle, variability and trends, 2000–2019, Elementa Science of the Anthropocene, 10, 00073, https://doi.org/10.1525/elementa.2021.00073, 2022.

Herman, A., Wojtysiak, K., and Moskalik, M.: Wind wave variability in Hornsund fjord, west Spitsbergen, Estuar. Coast. Shelf S., 217, 96–109, https://doi.org/10.1016/j.ecss.2018.11.001, 2019.

Herman, A., Swirad, Z. M., and Moskalik, M.: Increased exposure of the shores of Hornsund (Svalbard) to wave action due to a rapid shift in sea ice conditions, Elementa Science of the Anthropocene, 13, https://doi.org/10.1525/elementa.2024.00067, 2025.

Hersbach, H., Bell, B., Berrisford, P., Biavati, G., Horányi, A., Muñoz Sabater, J., Nicolas, J., Peubey, C., Radu, R., Rozum, I., Schepers, D., Simmons, A., Soci, C., Dee, D., and Thépaut, J.-N.: ERA5 hourly data on single levels from 1940 to present, Copernicus Climate Change Service Climate Data Store (CDS) [data set], https://doi.org/10.24381/cds.adbb2d47 (last access: 8 October 2025), 2023.

IPCC: Climate Change 2023: Synthesis Report. Contribution of Working Groups I, II and III to the Sixth Assessment Report of the Intergovernmental Panel on Climate Change, edited by: Core Writing Team, Lee, H., and Romero, J., IPCC, Geneva, Switzerland, 184 pp., https://doi.org/10.59327/IPCC/AR6-9789291691647, 2023.

Itkin, P., Losch, M., and Gerdes, R.: Landfast ice affects the stability of the Arctic halocline: Evidence from a numerical model, J. Geophys. Res.-Oceans, 120, 2622–2635, https://doi.org/10.1002/2014jc010353, 2015.

Jakacki, J., Przyborska, A., Kosecki, S., Sundfjord, A., and Albretsen, J.: Modelling of the Svalbard fjord Hornsund, Oceanologia, 59, 473–495, https://doi.org/10.1016/j.oceano.2017.04.004, 2017.

Jansen, E., Christensen, J. H., Dokken, T., Nisancioglu, K. H., Vinther, B. M., Capron, E., Guo, C., Jensen, M. F., Langen, P. L., Pedersen, R. A., Yang, S., Bentsen, M., Kjær, H. A., Sadatzki, H., Sessford, E., and Stendel, M.: Past perspectives on the present era of abrupt Arctic climate change, Nat. Clim. Change, 10, 714–721, https://doi.org/10.1038/s41558-020-0860-7, 2020.

Jensen, D., Mahoney, A., and Resler, L.: The annual cycle of landfast ice in the eastern Bering Sea, Cold Reg. Sci. Technol., 14, 103059, https://doi.org/10.1016/j.coldregions.2020.103059, 2020.

Johansson, A. M., Malnes, E., Gerland, S., Cristea, A., Doulgeris, A. P., Divine, D. V., Pavlova, O., and Lauknes, T. R.: Consistent ice and open water classification combining historical synthetic aperture radar satellite images from ERS-1/2, Envisat ASAR, RADARSAT-2 and Sentinel-1A/B, Ann. Glaciol., 61, 40–50, https://doi.org/10.1017/aog.2019.52, 2020.

Korhonen, M., Moskalik, M., Głowacki, O., and Jain, V.: Oceanographic monitoring in Hornsund fjord, Svalbard, Earth Syst. Sci. Data, 16, 4511–4527, https://doi.org/10.5194/essd-16-4511-2024, 2024.

Kowalik, Z., Marchenko, A., Brazhnikov, D., and Marchenko, N.: Tidal currents in the western Svalbard Fjords, Oceanologia, 57, 318–327, https://doi.org/10.1016/j.oceano.2015.06.003, 2015.

Kwok, R.: Contrasts in sea ice deformation and production in the Arctic seasonal and perennial ice zones,J. Geophys. Res., 111, C11S22, https://doi.org/10.1029/2005JC003246, 2006.

Larsen, Y., Engen, G., Lauknes, T., Malnes, E., and Høgda, K.: A generic differential interferometric SAR processing system, with applications to land subsidence and snow-water equivalent retrieval, Fringe 2005 Workshop, 610, ISBN 92-9092-921-9, 2006.

Lebedev, V.: Rost l'da v arkticheskikh rekakh i moriakh v zavisimosti ot otritsatel'nykh temperatur vozdukha, Problemy Arktiki, 5, 9–25, 1938.

Lei, R., Leppäranta, M., Cheng, B., Heil, P., and Li, Z.: Changes in ice-season characteristics of a European Arctic lake from 1964 to 2008, Clim. Change, 115, 725–739, https://doi.org/10.1007/s10584-012-0489-2, 2012.

Li, T., Hofer, S., Moholdt, G., Igneczi, A., Heidler, K., Zhu, X. X., and Bamber, J.: Pervasive glacier retreats across Svalbard from 1985 to 2023, Nat. Commun., 16, 705, https://doi.org/10.1038/s41467-025-55948-1, 2025.

Mahoney, A. R. and Einhorn, A. H.: The Evolving Decline of Landfast Sea Ice in Northern Alaska and Adjacent Waters: Results from an Updated Climatology, J. Geophys. Res.-Oceans, 131, e2025JC022464, https://doi.org/10.1029/2025JC022464, 2026.

Mahoney, A. R., Eicken, H., Gaylord, A. G., and Gens, R.: Landfast sea ice extent in the Chukchi and Beaufort Seas: The annual cycle and decadal variability, Cold Reg. Sci. Technol., 103, 41–56, https://doi.org/10.1016/j.coldregions.2014.03.003. 2014.

Mioduszewski, J., Vavrus, S., and Wang, M.: Diminishing Arctic Sea ice promotes stronger surface winds, J. Climate, 31, 8101–8119, https://doi.org/10.1175/jcli-d-18-0109.1, 2018.

Muckenhuber, S., Nilsen, F., Korosov, A., and Sandven, S.: Sea ice cover in Isfjorden and Hornsund, Svalbard (2000–2014) from remote sensing data, The Cryosphere, 10, 149–158, https://doi.org/10.5194/tc-10-149-2016, 2016.

NOAA: National Centers for Environmental Information, Climate at a Glance: Global Time Series, https://www.ncdc.noaa.gov/cag/, last access: 15 June 2025.

NPI: Kartdata Svalbard 1 : 100 000 (S100 Kartdata)/Map Data, Norwegian Polar Institute [data set], https://doi.org/10.21334/npolar.2014.645336c7, 2014.

Onarheim, I. H., Smedsrud, L. H., Ingvaldsen, R. B., and Nilsen, F.: Loss of sea ice during winter north of Svalbard, Tellus, 66A, 23933, https://doi.org/10.3402/tellusa.v66.23933, 2014.

Papin, V., Swirad, Z. M., Johansson, A. M., and Malnes, E.: Ice distribution in Hornsund fjord, Svalbard from Envisat ASAR (2002–2012), PANGAEA [data set], https://doi.org/10.1594/pangaea.986427, 2025a.

Papin, V., Swirad, Z. M., Johansson, A. M., and Malnes, E.: Ice distribution in Hornsund fjord, Svalbard from Sentinel-1A (2023–2025), PANGAEA [data set], https://doi.org/10.1594/PANGAEA.987853, 2025b.

Park, J.-W., Korosov, A. A., Babiker, M., Won, J.-S., Hansen, M. W., and Kim, H.-C.: Classification of sea ice types in Sentinel-1 synthetic aperture radar images, The Cryosphere, 14, 2629–2645, https://doi.org/10.5194/tc-14-2629-2020, 2020.

Pavlova, O., Gerland, S., and Hop, H.: Changes in sea ice extent and thickness in Kongsfjorden, Svalbard (2003–2016), in: The Ecosystem of Kongsfjorden, Svalbard, edited by: Hop, H. and Wiencke, C., Advances in Polar Ecology, 2, Springer, Cham, 105–136, https://doi.org/10.1007/978-3-319-46425-1_4, 2019.

Promińska, A., Falck, E., and Walczowski, W.: Interannual variability in hydrography and water mass distribution in Hornsund, an Arctic fjord in Svalbard, Polar Res., 37, 1495546, https://doi.org/10.1080/17518369.2018.1495546, 2018.

Rinke, A., Maturilli, M., Graham, R. M., Matthes, H., Handorf, D., Cohen, L., Hudson, S. R., and Moore, J. C.: Extreme cyclone events in the Arctic: Wintertime variability and trends, Environ. Res. Lett., 12, 094006, https://doi.org/10.1088/1748-9326/aa7def, 2017.

Sauser, C., Angelier, F., Blévin, P., Chastel, O., Gabrielsen, G. W., Jouanneau, W., Kato, A., Moe, B., Ramírez, F., Tartu, S., and Descamps, S.: Demographic responses of Arctic seabirds to spring sea-ice variations, Front. Ecol. Evol., 11, 1107992, https://doi.org/10.3389/fevo.2023.1107992, 2023.

Selyuzhenok, V., Mahoney, A., Krumpen, T., Castellani, G., and Gerdes, R.: Mechanisms of fast-ice development in the south-eastern Laptev Sea: a case study for winter of 2007/08 and 2009/10, Polar Res., 36, 1411140, https://doi.org/10.1080/17518369.2017.1411140, 2017.

Smith, T. G. and Lydersen, C.: Availability of suitable landfast ice and predation as factors limiting ringed seal populations, Phoca hispida, in Svalbard, Polar Res., 10, 585–594. https://doi.org/10.3402/polar.v10i2.6769, 1991.

Stocker, A. N., Renner, A. H. H., and Knol-Kauffman, M.: Sea ice variability and maritime activity around Svalbard in the period 2012–2019, Sci. Rep., 10, 17043, https://doi.org/10.1038/s41598-020-74064-2, 2020.

Strzelewicz, A., Przyborska, A., and Walczowski, W.: Increased presence of Atlantic Water on the shelf south-west of Spitsbergen with implications for the Arctic fjord Hornsund, Prog. Oceanogr., 200, 102714, https://doi.org/10.1016/j.pocean.2021.102714, 2021.

Su, H. and Wang, Y.: Using MODIS data to estimate sea ice thickness in the Bohai Sea (China) in the 2009–2010 winter, J. Geophys. Res., 117, C10018, https://doi.org/10.1029/2012JC008251, 2012.

Svendsen, H., Beszczynska-Møller, A., Hagen, J. O., Lefauconnier, B., Tverberg, V., Gerland, S., Ørbæk, J. B., Bischof, K., Papucci, C., Zajaczkowski, M., Azzolini, R., Bruland, O., and Wiencke, C.: The physical environment of Kongsfjorden–Krossfjorden, an Arctic fjord system in Svalbard, Polar Res., 21, 133–166, https://doi.org/10.3402/polar.v21i1.6479, 2002.

Swerpel, S.: The Hornsund Fiord: water masses, Pol. Polar Res., 6, 475–496, 1985.

Swirad, Z. M.: Correction to the "Ice distribution in Hornsund fjord, Svalbard from Sentinel-1A/B (2014–2023)" dataset, Zenodo [data set], https://doi.org/10.5281/zenodo.17350297, 2025.

Swirad, Z. M., Johansson, A. M., and Malnes, E.: Ice distribution in Hornsund fjord, Svalbard from Sentinel-1A/B (2014–2023), PANGAEA [data set], https://doi.org/10.1594/PANGAEA.963167, 2023a.

Swirad, Z. M., Moskalik, M., and Herman, A.: Wind wave and water level dataset for Hornsund, Svalbard (2013–2021), Earth Syst. Sci. Data, 15, 2623–2633, https://doi.org/10.5194/essd-15-2623-2023, 2023b.

Swirad, Z. M., Johansson, A. M., and Malnes, E.: Extent, duration and timing of the sea ice cover in Hornsund, Svalbard, from 2014–2023, The Cryosphere, 18, 895–910, https://doi.org/10.5194/tc-18-895-2024, 2024a.

Swirad, Z. M., Johansson, A. M., and Malnes, E.: Ice distribution in Hornsund fjord, Svalbard from RADARSAT-2 (2012–2016), PANGAEA [data set], https://doi.org/10.1594/PANGAEA.969031, 2024b.

Swirad, Z., Herman, A., and Moskalik, M.: Sub-monthly to inter-annual Arctic gravel beach change and controlling factors, EGU General Assembly 2026, Vienna, Austria, 3–8 May 2026, EGU26-2311, https://doi.org/10.5194/egusphere-egu26-2311, 2026a.

Swirad, Z. M., Johansson, A. M., and Malnes, E.: Distribution of landfast, drift and glacier ice in Hornsund, Svalbard, The Cryosphere, 20, 113–134, https://doi.org/10.5194/tc-20-113-2026, 2026b.

van den Broek, D., Urbancic, G. H., Rantanen, M., and Vihma, T.: Svalbard's record-breaking arctic summer 2024: Anomalies beyond climatological warming trends, Geophys. Res. Lett., 52, e2025GL115015, https://doi.org/10.1029/2025GL115015, 2025.

Wakabayashi, H., Matsuoka, T., Nakamura, K., and Nishio, F.: Polarimetric Characteristics of sea ice in the sea of Okhotsk observed by airborne L-band SAR, IEEE T. Geosci. Remote, 42, 2412–2425, https://doi.org/10.1109/TGRS.2004.836259, 2004.

Wawrzyniak, T. and Osuch, M.: A 40-year High Arctic climatological dataset of the Polish Polar Station Hornsund (SW Spitsbergen, Svalbard), Earth Syst. Sci. Data, 12, 805–815, https://doi.org/10.5194/essd-12-805-2020, 2020.

Wojtysiak, K., Herman, A., and Moskalik, M.: Wind wave climate of west Spitsbergen: seasonal variability and extreme events, Oceanologia, 60, 331–343, https://doi.org/10.1016/j.oceano.2018.01.002, 2018.

Zagórski, P., Rodzik, J., Moskalik, M., Strzelecki, M. C., Lim, M., Błaszczyk, M., Promińska, A., Kruszewski, G., Styszyńska, A., and Malczewski, A.: Multidecadal (1960–2011) shoreline changes in Isbjørnhamna (Hornsund, Svalbard), Pol. Polar Res., 36, 369–390, 2015.

Zakhvatkina, N., Korosov, A., Muckenhuber, S., Sandven, S., and Babiker, M.: Operational algorithm for ice–water classification on dual-polarized RADARSAT-2 images, The Cryosphere, 11, 33–46, https://doi.org/10.5194/tc-11-33-2017, 2017.